Technische
Universität
München

Walther - Meißner -
Institut für Tief -
Temperaturforschung

Bayerische
Akademie der
Wissenschaften

Optimized geometry for a compact 3D quantum memory

Master's Thesis

Julia Lamprich

Supervisor: Priv.-Doz. Dr. Habil. Frank Deppe

October 23, 2020

Fakultät für Physik
Technische Universität München

Abstract

Quantum computing is one of the most promising technologies in today's research providing major improvements in computational speedup and cryptography.
To realize a quantum computer it has to be possible to manipulate, store and read out different quantum states. These tasks can be reached by coupling a transmon qubit capacitively to two distinct modes of a single 3D cavity. Then a mode with high Q-factor is used for long storage and another mode with low Q-factor is used for fast readout. In this design manipulation of the qubit states via microwave signals is reached through the readout port of the cavity.
The goal of this thesis is to design, optimize and finally test a new geometry for such a 3D quantum memory using a horseshoe architecture. The first part consists of a simulation part, where the cavity design is created and optimized. Subsequently, the new cavity is experimentally tested at cryogenic temperatures. To thoroughly analyze the characteristics of the cavity and the qubit, measurements with and without the qubit are carried out. As a final step a quantum memory protocol is implemented.

Contents

Chapter 1

Introduction

Since Konrad Zuse built the first Z1 in 1938 [1], the working principle of a computer consists of manipulating, storing and reading out information. Until today, computers have become more and more powerful by increasing the number of transistors while simultaneously decreasing their size. But still there are certain problems that cannot be solved on such a classical computer within human timescales.
A promising solution is the quantum computer which is theoretically proven to allow for an exponential speedup for certain problems such as prime factorization [2]. Recently, Google has provided the first experimental evidence for quantum supremacy [3]. With 53 superconducting qubits, they solved a specific problem in 200 seconds, whereas a state-of-the-art classical supercomputer would have taken about 10 000 years. Despite its impressive character, this achievement can only be considered as the fulfillment of an intermediate milestone in the research field of quantum computing. For instance, to perform Shor's algorithm to factorize a 1000 bit number, a few hundreds of millions of qubits are needed [4].
Furthermore, in reality, a quantum system is never completely isolated from the environment, so uncontrolled interactions can appear between the qubits and the environment [5]. As a consequence, quantum effects are not observable anymore after a characteristic timescale called the decoherence time. So, future research activities have to strive towards fully fault-tolerant quantum computing [6].
When this goal is reached, quantum computing will not only be able to outperform classical computers, but will also be a major resource for applications such as quantum communication [7, 8] and quantum cryptography [9].
One of the most successful physical realizations of quantum computing is the field of circuit quantum electrodynamics, where a superconducting artificial atom, i.e., the qubit, is coupled to a cavity [10]. A major advantage is that the environment does not directly couple to the qubit, so the noise is reduced and the lifetime of the

qubit extended [11]. The cavity can serve two functionalities: as readout and as memory device for the qubit information. Due to its technological simplicity, the cavity lends itself to act as a long-lived storage device for quantum information.
Besides such a quantum memory, which would be provided by a perfectly isolated system, a fast readout is also needed for building a computer. These two goals are apparently contradictory when trying to implement them with a single cavity mode. So, one solution to achieve fast readout and long-lived storage simultaneously is to couple two cavities to the qubit, one with a low Q-factor for readout and one with a high Q-factor for storage [12]. As this solution is very bulky, one can also use the multimode structure of a cavity to couple the qubit to two distinct modes of a single cavity. The result is a compact and scalable quantum memory which has already been investigated by E. Xie *et al.* [13, 14]. They use a rectangular 3D microwave cavity and a transmon qubit to realize the quantum memory. Notably, 3D microwave resonators are known to currently outperform their 2D counterparts, reaching millisecond coherence [15].
However, the rectangular cavity design also comes with some difficulties [13]. Hence, the goal of this thesis is to replace the simple rectangular cavity design and create an optimized geometry for a 3D quantum memory using a horseshoe architecture. The theoretical background necessary for that is given in Chapter 2. Here, the properties of cavity and qubit and the coupling between them are introduced. Chapter 3 presents the simulation part of this work, where the cavity is designed and optimized with respect to fast readout and long storage times. In order to test the final horseshoe design it is built by the workshop at WMI. The experimental techniques needed for the measurement part including the setup, frequency domain measurements and pulse protocols for time domain measurements are explained in Chapter 4. Chapter 5 finally states the measurement results obtained from the horseshoe cavity excluding and including qubit chips. It is shown that the new geometry basically works as a quantum memory and that a quantum memory protocol can be implemented. In Chapter 6, the results are summarized and further improvements for the cavity design are discussed.

Chapter 2

Theory

2.1 3D microwave cavity

In general, a 3D cavity is a closed hollow geometry that restricts the electromagnetic field to certain boundary conditions due to the metallic walls. Comparable to an optical cavity, where light is reflected back and forth between two mirrors, in this case microwaves bounce back and forth between the walls of the cavity thus being confined to the cavity. These electromagnetic waves can be described by transverse electric (TE) and transverse magnetic (TM) modes where the electric and magnetic fields oscillate perpendicular to the direction of propagation and to each other. Only certain modes fulfill the boundary conditions, such as $\vec{E}_\mathrm{t} = 0$ at the position of the walls. These modes represent standing waves inside the cavity oscillating at geometry-dependent eigenfrequencies. The mode with the lowest eigenfrequency is referred to as the fundamental mode or TE101 mode. In case of a rectangular cavity the different modes are straightforward to calculate [16]. For more complex structures, such as the horseshoe geometry discussed in this thesis, a simulation software has to be used. Figure 2.1 shows the first electric and magnetic mode of this geometry simulated with CST Microwave Studio [17].
Quantum mechanically the cavity modes can be described by the Hamiltonian of a harmonic oscillator [18]:

$$\hat{H} = \hbar\omega_\mathrm{c}(\hat{a}^\dagger\hat{a} + \frac{1}{2}), \tag{2.1}$$

with the cavity frequency ω_c and the photon creation and annihilation operators $\hat{a}^\dagger$ and $\hat{a}$.

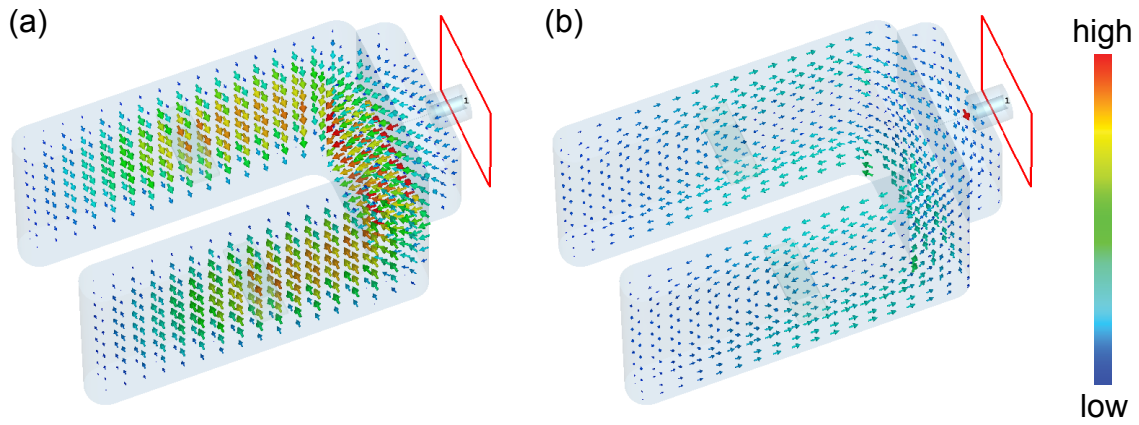

Figure 2.1: (a) First electric and (b) first magnetic mode of the horseshoe geometry. The red rectangle marks the input and output port. The color code shows the field strength in arbitrary units, the arrows indicate the field orientation.

2.1.1 Quality factor

A measure for the total energy loss of the cavity is given by the loaded Q-factor, which is defined as the ratio of total energy to dissipated energy [16]:

$$Q_{\mathrm{L}} = \frac{\hbar\omega_{\mathrm{c}}}{\hbar\Delta\omega} = \frac{f_{\mathrm{c}}}{\Delta f}. \tag{2.2}$$

Here $f_{\mathrm{c}} = \omega_{\mathrm{c}}/2\pi$ accounts for the cavity's resonance frequency and $\Delta f = \Delta\omega/2\pi$ for the full width at half maximum (FWHM) of the power spectrum. One differentiates between external and internal losses quantified by external and internal Q-factors Q_{x} and Q_0 or external and internal loss rates κ_{x} and κ_0:

$$\frac{1}{Q_{\mathrm{L}}} = \frac{1}{Q_{\mathrm{x}}} + \frac{1}{Q_0} = \frac{\kappa_{\mathrm{x}} + \kappa_0}{2\pi f_{\mathrm{c}}}. \tag{2.3}$$

Details on which effects are responsible for either of them are discussed in the next two sections.

If the external Q-factor is larger than the internal one the system is undercoupled. On the other hand, if the internal quality factor is larger than the external one the system is overcoupled. In case external and internal quality factors are equal the system is critically coupled.

2.1.2 External losses

External losses of the cavity occur due to the coupling to output ports. In this thesis a dipole antenna which simultaneously serves as input and output port is used for electric field coupling. The rate of photons which leave the cavity through the antenna is then given by the external coupling rate κ_{x}:

$$\kappa_{\mathrm{x}} = \frac{\vec{p} \cdot \vec{E}}{\hbar}. \tag{2.4}$$

Inserting the dipole moment $\vec{p} = q\vec{l_{\mathrm{ant}}}$ with the length of the antenna l_{ant} and the charge $q = C_{\mathrm{x}} \int E_{||,\,\mathrm{ant}} dx$, where C_{x} is the coupling capacitance and $E_{||,\,\mathrm{ant}}$ is the electric field parallel to the antenna, the coupling rate can be rewritten as [14]:

$$\kappa_{\mathrm{x}} = \frac{C_{\mathrm{x}}}{\hbar} \Big(\int E_{||,\,\mathrm{ant}}\ dx \Big)^2. \tag{2.5}$$

A measure for the total energy loss caused by the coupling to the output antenna is given by the external Q-factor from Eq. (2.3) which is proportional to $1/\kappa_{\mathrm{x}}$.

2.1.3 Internal losses

The internal losses which mainly determine the internal Q-factor are surface losses and losses due to the insertion of a dielectric:

$$\frac{1}{Q_0} = \frac{1}{Q_{\mathrm{surf}}} + \frac{1}{Q_{\mathrm{diel}}}. \tag{2.6}$$

Surface losses are caused by surface currents induced by the magnetic field tangential to the surface [16]. It can be shown that the Q-factor Q_{surf} is proportional to the inverse of the surface resistance. As in this thesis a superconducting cavity is used, the surface resistance is very low, providing a high Q_{surf}.
Dielectric losses arise as the qubit is placed inside the cavity on a silicon chip. A lower bound for the Q-factor Q_{diel} can be calculated to [16]:

$$\frac{1}{\tan(\delta)} < Q_{\mathrm{diel}}, \tag{2.7}$$

with $\tan(\delta)$ being the loss tangent of the dielectric. Equality holds when the cavity is completely filled with the dielectric. In addition to an energy loss the insertion of a dielectric leads to a slight downshift of the cavity's resonance frequency due to the change in permittivity. For the case of a simple rectangular cavity and typical

dimensions the shift accounts to 4 % [14].

2.2 Superconducting transmon qubit

2.2.1 Qubits

Quantum bits, usually referred to as qubits, can be implemented with any well defined two-level quantum system. As in most real systems higher levels also exist, it is important that these higher levels are not excited during qubit manipulations [19]. So higher level states should be well separated from ground and excited state. Natural examples for quantum two-level systems are spin-1/2 systems [20] or light of different polarizations. [21]. In this thesis superconducting circuits provide the two-level system for the qubit.
Different from classical bits, which either have the value "0" or "1", a qubit can be in an arbitrary superposition of two basis states:

$$|\psi\rangle = \alpha\,|g\rangle + \beta\,|e\rangle\,. \tag{2.8}$$

Here α and β are complex numbers. After a measurement, the qubit would be in the ground state with probability $|\alpha^2|$ and in the excited state with probability $|\beta^2|$. As the total probability should add up to unity, α and β have to satisfy the normalization condition $|\alpha^2| + |\beta^2| = 1$. Thus all qubit states can be visualized on the surface of a unit sphere, the Bloch sphere. In the Bloch sphere representation the qubit state can be rewritten as [22]:

$$|\psi\rangle = \cos\frac{\theta}{2}\,|g\rangle + e^{i\varphi}\sin\frac{\theta}{2}\,|e\rangle\,, \tag{2.9}$$

with the polar angle $0 \leq \theta \leq \pi$ and the azimuthal angle $0 \leq \varphi \leq 2\pi$. A graphical illustration of the Bloch sphere is depicted in Fig. 2.2.
Rotations of the qubit state about the coordinate axes of the Bloch sphere are described using the Pauli matrices:

$$\hat{\sigma}_\mathrm{x} \equiv \begin{pmatrix} 0 & 1 \\ 1 & 0 \end{pmatrix} \qquad \hat{\sigma}_\mathrm{y} \equiv \begin{pmatrix} 0 & -i \\ i & 0 \end{pmatrix} \qquad \hat{\sigma}_\mathrm{z} \equiv \begin{pmatrix} 1 & 0 \\ 0 & -1 \end{pmatrix}\,. \tag{2.10}$$

Using the Pauli z-matrix, the qubit Hamiltonian can be written as:

$$\hat{H}_{\mathrm{q}} = \hbar\omega_{\mathrm{q}}\hat{\sigma}_{\mathrm{z}}. \tag{2.11}$$

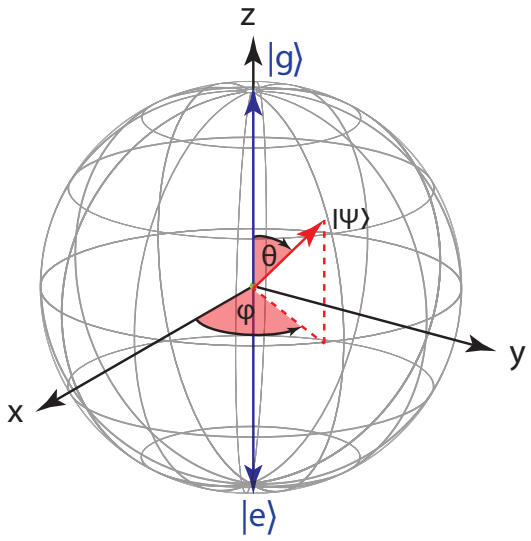

Figure 2.2: Bloch sphere representation of the qubit state $|\psi\rangle$.

2.2.2 Josephson junction

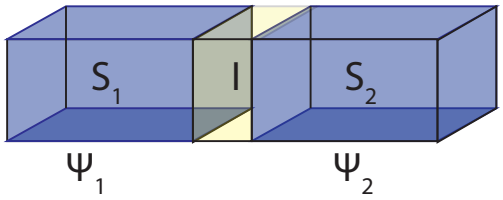

Figure 2.3: Two superconductors S_1 and S_2 separated by a thin insulator I form a Josephson junction. The superconducting state is described by the macroscopic wave functions ψ_1 and ψ_2.

Since a harmonic oscillator such as the one provided by an LC-circuit is a linear system, it alone cannot be used as a qubit (see Sec. 2.2.1). However, if an anharmonicity is added the system turns out to be nonlinear, providing the toolkit for the creation of a qubit. In circuit quantum electrodynamics a Josephson junction is used as an anharmonicity. It consists of two superconductors separated by a thin insulating barrier as schematically shown in Fig. 2.3. This construction gives rise to

the Josephson effect [23], which is described by the two Josephson equations:

$$I_\mathrm{s} = I_\mathrm{c} \sin\varphi, \tag{2.12}$$

$$\frac{\partial\varphi}{\partial t} = \frac{2\pi}{\phi_0} V. \tag{2.13}$$

To better understand the physical meaning of these equations, we introduce the superconducting state, which is fully described by macroscopic wave functions of the form $\psi = \sqrt{n_\mathrm{s}} e^{i\Theta}$. Here n_s refers to the density of superconducting electrons and Θ is the phase.

The first Josephson equation [cf. Eq. (2.12)] states that, in the absence of any potential, the supercurrent through a Josephson junction varies sinusoidal with the phase difference $\varphi = \Theta_2 - \Theta_1$. The critical current I_c defines the current below which the system is in the superconducting state.

According to the second Josephson equation [cf. Eq. (2.13)], an externally applied voltage across the junction leads to a change of the phase difference φ in time.

The Josephson junction stores a finite energy which can be considered as a binding energy due to the overlap of the two macroscopic wave functions. This energy is called the Josephson coupling energy and is given by:

$$E_\mathrm{pot} = \frac{\phi_0 I_\mathrm{c}}{2\pi}(1 - \cos\varphi) = E_\mathrm{J}(1 - \cos\varphi). \tag{2.14}$$

Furthermore, there is a kinetic energy as the two separated superconductors can be seen as a capacitance. This so-called charging energy is given by

$$E_\mathrm{kin} = \frac{Q^2}{2C} = 4E_\mathrm{C}N^2, \tag{2.15}$$

with charge Q, number of Cooper pairs $N = \frac{Q}{2e}$ and capacitance C.

To describe the system quantum mechanically, a canonical quantization $N \to \hat{N} = -i\frac{\partial}{\partial\hat{\varphi}}$ and $\varphi \to \hat{\varphi}$ has to be performed.

Josephson energy and charging energy define the operation regime of the Josephson junction. The cosine in the Josephson energy makes the junction nonlinear so that it provides the required anharmonicity for the creation of a qubit.

2.2.3 Transmon qubit

The transmon qubit (transmission line shunted plasma oscillation qubit) is currently the most successful qubit with respect to coherence times [24]. Its geometry is mainly adopted from the Cooper pair box (CPB), but the ratio of Josephson energy to charging energy at which it is operated is different. The CPB uses the charge regime where $E_C \gg E_J$, but encounters the problem that it is very sensitive to charge noise. As the charge dispersion decreases exponentially with increasing E_J/E_C while the loss of anharmonicity obeys a weak power law, the transmon qubit operates at $E_J/E_C \approx 50$. Consequently, the charge noise sensitivity is reduced significantly while maintaining an anharmonicity large enough to realize a two-level system.

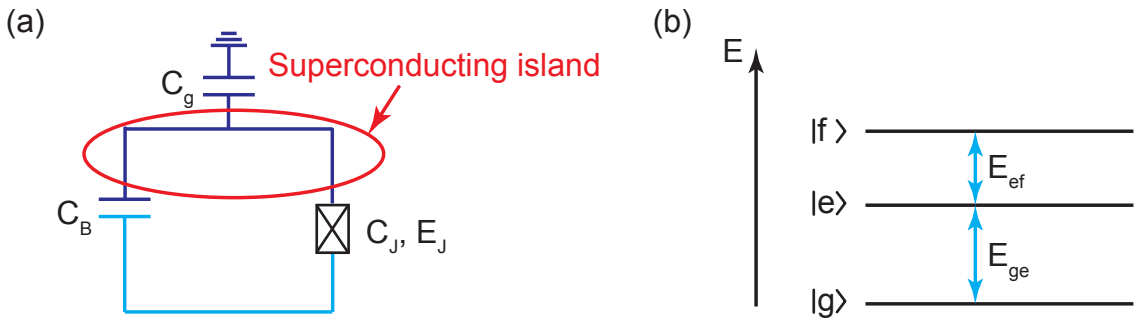

Figure 2.4: (a) Circuit representation of the transmon qubit. The transmon qubit consists of a Josephson junction with capacitance C_J and Josephson energy E_J, a large shunting capacitance C_B and capacitance to ground C_g. (b) Energy level scheme of the transmon qubit.

As depicted in Fig. 2.4, the transmon qubit consists of a Josephson junction with capacitance C_J and Josephson energy E_J, a large shunting capacitance C_B and capacitance to ground C_g. The charging energy can be seen as the energy required to add each electron of a Cooper pair to the island. So the total capacitance that contributes to the charging energy is a parallel connection of C_B and C_J connected in series to the ground capacitance C_g, which accounts to $C_\Sigma = C_g(C_B + C_J) / (C_B + C_J + C_g)$ [25]. The Hamiltonian is given by:

$$\hat{H} = 4E_C(\hat{N} - \hat{N}_g)^2 - E_J \cos\hat{\varphi}. \tag{2.16}$$

Solving this Hamiltonian with perturbation theory leads to the following first two

transition energies E_{ge} and E_{ef} and the anharmonicity α [26]:

$$E_{ge} = E_1 - E_0 \approx \sqrt{8E_C E_J} - E_C, \tag{2.17}$$

$$E_{ef} = E_2 - E_1 \approx \sqrt{8E_C E_J} - 2E_C, \tag{2.18}$$

$$\alpha \equiv E_{ef} - E_{ge} \approx -E_C. \tag{2.19}$$

2.3 Compact 3D quantum memory

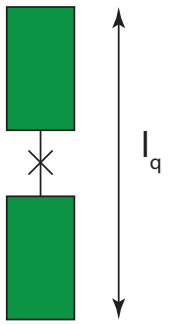

Figure 2.5: Sketch of the transmon qubit. The shunting capacitance is illustrated by the two paddles and serves as an electric dipole antenna with length l_q. The Josephson junction is represented by the cross.

The large shunting capacitance of the transmon qubit can be seen as an electric dipole antenna of length l_q which is depicted in Fig. 2.5. So a transmon qubit placed inside a cavity couples to the cavity electric field parallel to l_q with coupling constant [14]:

$$g = \frac{-2e\vec{l_q} \cdot \vec{E}_{rms}}{\hbar}. \tag{2.20}$$

Here $\vec{E}_{rms}$ is the root mean square of the vacuum electric field.
The qubit used in this thesis operates in the strong coupling regime where the coupling constant g is much larger than the qubit decay rate γ and the cavity decay rate κ:

$$g \gg \gamma, \kappa. \tag{2.21}$$

Furthermore, the coupling constant g is much smaller than the cavity and qubit eigenfrequencies ω_c and ω_q:

$$g \ll \omega_c, \omega_q. \tag{2.22}$$

Considering these conditions the system can be described with the Jaynes-Cummings Hamiltonian [11]:

$$\hat{H}_{JC} = \hbar\omega_c(\hat{a}^\dagger\hat{a} + \frac{1}{2}) + \frac{\hbar\omega_q}{2}\hat{\sigma}_z + \hbar g(\hat{a}\hat{\sigma}_+ + \hat{a}^\dagger\hat{\sigma}_-), \tag{2.23}$$

which is the sum of a resonator, qubit and interaction term, respectively.

2.3.1 The dispersive regime

Control and readout of the transmon qubit with the help of the cavity can be achieved by operating the system in the dispersive regime [11]. Here, the detuning Δ between the eigenfrequencies of qubit and cavity is much larger than the coupling constant g:

$$\Delta = \omega_q - \omega_c \gg g. \tag{2.24}$$

To see what exactly happens in this regime and why it is so useful a unitary transformation $\hat{U} = \exp(g/\Delta(\hat{a}\hat{\sigma}_+ - \hat{a}^\dagger\hat{\sigma}_-))$, which cancels the cavity–qubit interaction to lowest order, is performed. Expanding the transformed Hamiltonian to second order in g/Δ yields the following result [11]:

$$\hat{U}\hat{H}_{JC}\hat{U}^\dagger \approx \hbar(\omega_c + \underbrace{\frac{g^2}{\Delta}\hat{\sigma}_z}_{\substack{\text{AC Stark}\\ \text{shift}}})\hat{a}^\dagger\hat{a} + \frac{\hbar}{2}(\omega_q + \underbrace{\frac{g^2}{\Delta}}_{\substack{\text{Lamb}\\ \text{shift}}})\hat{\sigma}_z. \tag{2.25}$$

The presence of the qubit causes a dispersive shift χ of the cavity frequency depending on the qubit state

$$\tilde{\omega_c} = \omega_c + \frac{g^2}{\Delta}\hat{\sigma}_z \equiv \omega_c + \chi\hat{\sigma}_z, \tag{2.26}$$

which is called the AC Stark effect. Therefore a measurement of the transmission amplitude or phase of the cavity provides information on the qubit state.
As the transmon qubit is no perfect two-level system, contributions of higher energy levels result in an effective Hamiltonian [26]:

$$\hat{H}_{eff} = \frac{\hbar\omega_q'}{2}\hat{\sigma}_z + \hbar(\omega_c' + \chi'\hat{\sigma}_z)\hat{a}^\dagger\hat{a}, \tag{2.27}$$

with a renormalized qubit transition and cavity resonance frequency $\omega_q' = \omega_q + \chi_{01}$ and $\omega_c' = \omega_c - \chi_{12}/2$. The effective dispersive shift χ' which is measured experimentally is given by:

$$\chi' = \chi_{01} - \frac{\chi_{12}}{2}, \tag{2.28}$$

with $\chi_{ij} \equiv g_{ij}^2/(\omega_{ij} - \omega_c)$. Here, $\omega_{ij} = \omega_j - \omega_i$ are the frequency differences between the different energy levels, while the transition from ground state to excited state ω_{01} is defined as the qubit frequency ω_q. The coupling of the cavity to higher levels of the qubit increases as $g_{i,i+1} \approx \sqrt{i+1}\, g$ while g is the coupling to the transition of ground and excited state.
With the definition of the anharmonicity α from Eq. (2.19) the effective dispersive shift can be rewritten as:

$$\chi' \approx \frac{g^2}{\Delta} \frac{\alpha}{\hbar\Delta + \alpha} = \chi_{01} \frac{\alpha}{\hbar\Delta + \alpha} \tag{2.29}$$

2.3.2 AC Stark shift

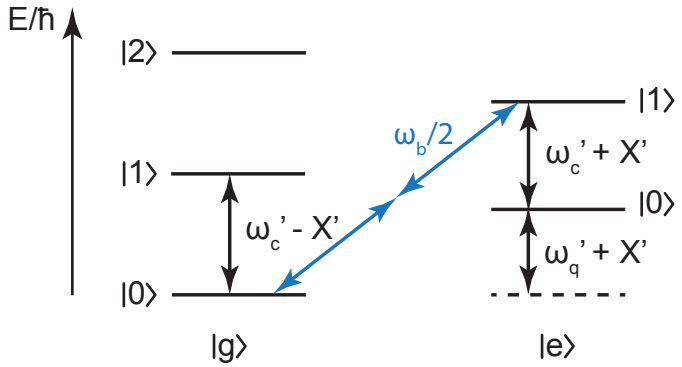

Figure 2.6: Energy spectrum of a coupled qubit–cavity system in the dispersive regime. The blue arrows indicate the blue sideband (BSB) transition which can be driven via a two-photon process.

As discussed in Sec. 2.3.1, the coupling of the qubit to the radiation field of the cavity shifts the resonator frequency which is used for dispersive readout of the qubit state [27]. Correspondingly, the resonator also influences the qubit. This influence can be seen by rearranging the terms of the Hamiltonian in Eq. (2.25) which gives rise to a shifted qubit frequency $\tilde{\omega}_q$ [28]:

$$\tilde{\omega}_q = \omega_q + 2n\chi' + \chi'. \tag{2.30}$$

The second term corresponds to an AC Stark shift proportional to the photon number $n = \langle \hat{a}^\dagger \hat{a} \rangle$ inside the cavity and the third term corresponds to a Lamb shift due to the coupling to vacuum fluctuations.
The resulting energy level scheme of the dispersively coupled qubit–cavity system is depicted in Fig. 2.6.

2.3.3 Control of qubit–cavity system

In order to manipulate and control the qubit–cavity system, it is driven with coherent microwave pulses via the antenna port. Depending on frequency, power and length of these pulses different operations can be performed. As mentioned in Sec. 2.3.1, driving the system near the cavity resonance frequency leads to a measurement of the qubit state. On the other hand, irradiation close to the qubit resonance frequency allows to control the qubit state, for instance the qubit can be driven from the ground state to the excited state.
An external microwave drive that enters the resonator via the antenna port can be described by the Hamiltonian [11, 29]:

$$\hat{H}_\mathrm{D} = \hbar\Omega_\mathrm{d}(\hat{a}^\dagger e^{-i\omega_\mathrm{d}t} + \hat{a}e^{+i\omega_\mathrm{d}t}), \tag{2.31}$$

with the amplitude Ω_d and the frequency ω_d. Here, the actually applied oscillating drive is approximated by a rotating drive.
The total Hamiltonian of the system is then given by the Jaynes-Cummings Hamiltonian from Eq. (2.23) plus the drive:

$$\hat{H} = \hat{H}_\mathrm{JC} + \hat{H}_\mathrm{D}. \tag{2.32}$$

To examine the effect of the drive on the qubit–cavity system, the Hamiltonian is transformed to a displaced frame which cancels the driving term [30]. Here the unitary is the displacement operator [31]:

$$D(\alpha) = \exp(\alpha\hat{a}^\dagger - \alpha^*\hat{a}), \tag{2.33}$$

which transforms the Hamiltonian to:

$$\begin{aligned}\hat{H} &\to \hat{D}\hat{H}\hat{D}^\dagger + i\hbar\dot{\hat{D}}\hat{D}^\dagger \\ &= \hbar\omega_\mathrm{c}\hat{a}^\dagger\hat{a} + \hbar\frac{\omega_\mathrm{q}}{2}\hat{\sigma}_\mathrm{z} + \hbar g(\hat{a}\hat{\sigma}_+ + \hat{a}^\dagger\hat{\sigma}_-) + \hbar g(-\alpha\hat{\sigma}_+ - \alpha^*\hat{\sigma}_-),\end{aligned} \tag{2.34}$$

where $\alpha(t)$ has been chosen such that the driving term in the resulting Hamiltonian vanishes. An explicit calculation of the displaced frame transformation is shown in App. A. Moving the Hamiltonian from Eq. (2.34) to a frame rotating at frequency ω_d for both the qubit and the field operators and dropping any transient in $\alpha(t)$ leads to:

$$\hat{H} = \hbar\Delta_\mathrm{c}\hat{a}^\dagger\hat{a} + \hbar\frac{\Delta_\mathrm{q}}{2}\hat{\sigma}_\mathrm{z} + \hbar g(\hat{a}\hat{\sigma}_+ + \hat{a}^\dagger\hat{\sigma}_-) + \hbar\frac{\Omega_\mathrm{R}}{2}\hat{\sigma}_\mathrm{x}. \tag{2.35}$$

Here $\Delta_\mathrm{c} = \omega_\mathrm{c} - \omega_\mathrm{d}$ is the detuning between cavity and drive, $\Delta_\mathrm{q} = \omega_\mathrm{q} - \omega_\mathrm{d}$ is the detuning between qubit transition frequency and drive, and Ω_R is the Rabi frequency defined by:

$$\Omega_\mathrm{R} = 2\frac{\Omega_\mathrm{d} g}{\Delta_\mathrm{c}}. \tag{2.36}$$

From this Hamiltonian, the effect of an external drive can be seen directly: A drive near the qubit transition frequency leads to a rotation of the qubit Bloch vector about the $\hat{\mathrm{x}}$-axis. This phenomenon is called Rabi oscillation, because the qubit state oscillates between the ground and excited state with the Rabi frequency. So, depending on the pulse length of the drive, the qubit can be prepared in any possible azimuthal angle. For instance, a pulse that excites the qubit from the ground state to the excited state is called a π-pulse.

It is also possible to apply a drive at the sum of qubit and cavity frequency, thus creating a photon in the cavity and an excitation in the qubit [32]. This transition is called the blue sideband (BSB) transition which is depicted in Fig. 2.6. Due to parity conservation, the BSB transition is a two photon process [33, 34].

2.4 Quantum coherence and decoherence

As in reality the environment interacts with the qubit, quantum effects are not observable anymore after a characteristic time. The excited state decays exponentially to the ground state on a time scale T_1, which is referred to as energy relaxation time. Furthermore, after the dephasing time T_φ, the phase information of the qubit is lost. In real systems both energy relaxation and dephasing occur simultaneously. The decoherence time T_2 is related to the energy relaxation time and dephasing time via the following formula [35]:

$$\frac{1}{T_2} = \frac{1}{2T_1} + \frac{1}{T_\varphi}. \tag{2.37}$$

2.4.1 Purcell effect

As the cavity provides a different environment compared to an open system, it influences the lifetime of the qubit excited state. This phenomenon is called the Purcell effect. In other words, the presence of the cavity can enhance or suppress the spontaneous emission of the qubit depending on the detuning between qubit and cavity. The dispersive regime, where qubit and cavity are far detuned (see Sec. 2.3.1), suppresses the spontaneous qubit emission so the cavity protects the qubit excited state from decaying [36]. The qubit decays with the so called Purcell decay rate:

$$\kappa_{\mathrm{P}} = \left(\frac{g}{\Delta}\right)^2 \kappa, \tag{2.38}$$

where $\kappa = 2\pi\Delta f$ is the average photon loss rate.
As the cavity is a multimode 3D cavity, a better description of the Purcell decay rate is given by [37]:

$$\kappa_{\mathrm{P}}^{\mathrm{3D}} = \frac{Re[Y(\omega)]}{2\pi C_{\Sigma}}, \tag{2.39}$$

where the cavity admittance $Y(\omega)$ can be obtained by a CST simulation.

Chapter 3

Horseshoe memory architecture

This chapter focuses on the design and optimization of the horseshoe quantum memory. Simulations are performed with the finite-element method simulator CST Microwave Studio [17], which is a powerful tool for electromagnetic field simulations in the microwave frequency range. Within the scope of this thesis it is used to model a 3D horseshoe cavity and optimize its geometric parameters with respect to the requirements of a compact quantum memory:

- The electromagnetic mode structure of the cavity should provide one mode appropriate for readout and another mode for storage purposes. The corresponding optimization consists of maximizing the external Q-factor of the storage mode and minimizing the external Q-factor of the readout mode.

- Qubits should be positioned in such a way that they couple to both readout and storage mode.

3.1 Limitations of simple rectangular architecture

A rectangular cavity is the simplest design for an easily accessible multimode structure where the overcoupled TE101 mode is used for dispersive readout and the undercoupled TE201 mode is used for information storage [13]. However, there are several limitations regarding the rectangular design. For instance, the external quality factor of the storage mode, which should be as high as possible is very sensitive to antenna positioning inaccuracy. If the antenna is displaced by only 0.14 mm from the optimal position, the external Q-factor of the storage mode decreases to the level of the internal Q-factor [14]. Thus the overcoupled regime is reached leading to a faster qubit decay and lower storage times.

Furthermore, the frequency of the next higher cavity mode is very close to the storage mode frequency; the frequency gap is only about 45 MHz [14]. An undesired excitation of the next higher mode instead of the storage mode would also lead to shorter storage times as the next higher mode is strongly coupled to the antennas. To overcome these limitations, the aim of this thesis is to design and test the horseshoe geometry as a 3D quantum memory.

3.2 Finite-element simulations of the horseshoe geometry

The common CST workflow in a first step creates the structure to be modeled, determines the corresponding materials and defines a waveguide port where energy enters and leaves. Then, a mesh is created and the simulation engine can be started. To determine the electric and magnetic eigenfrequencies with corresponding field distributions of the structure, CST provides the eigenmode solver. This solver is also able to calculate external and internal Q-factors. To optimize different model parameters for a specific goal, the optimizer can be used. Another useful tool is provided by the parametric sweep. Here, the simulation results can be shown for different values of a specific geometric parameter. Another solver used in this thesis is the frequency solver. The results of this simulation yield the scattering parameters of the structure.

For all parameter simulations, the 3D horseshoe geometry is modeled as a vacuum surrounded by a perfect electrical conductor (PEC), as shown in Fig. 3.1 (a). As CST is not able to simulate a superconductor, cavity casing and antenna pin are always simulated as PEC. In reality, the cavity casing is fabricated from aluminum with a purity of 99.99 %. The cavity is operated well below the superconducting transition temperature which justifies the PEC approximation. Transmon qubit chips are simulated as a silicon brick of corresponding size with $\epsilon_r = 11.9$ and $\mu_r = 1$. The CST material library provides two different types of silicon: "silicon lossy" with a finite electric conductivity and "silicon loss free". In experiment, high resistivity silicon with a natural silicon oxide layer[1] is used. At low temperatures, silicon behaves as an insulator with vanishing electric conductivity. However, as the simulation assumes a perfect dielectric whereas in reality the silicon substrate certainly contains a finite amount of defects, simulations are performed with both "silicon lossy" and "silicon

[1] CrysTec GmbH Kristalltechnologie

loss free" chips.
The final cavity design is then imported as a CAD drawing to CST [cf. Fig. 3.1 (b)] to conduct a final simulation check before the cavity is fabricated by the workshop.

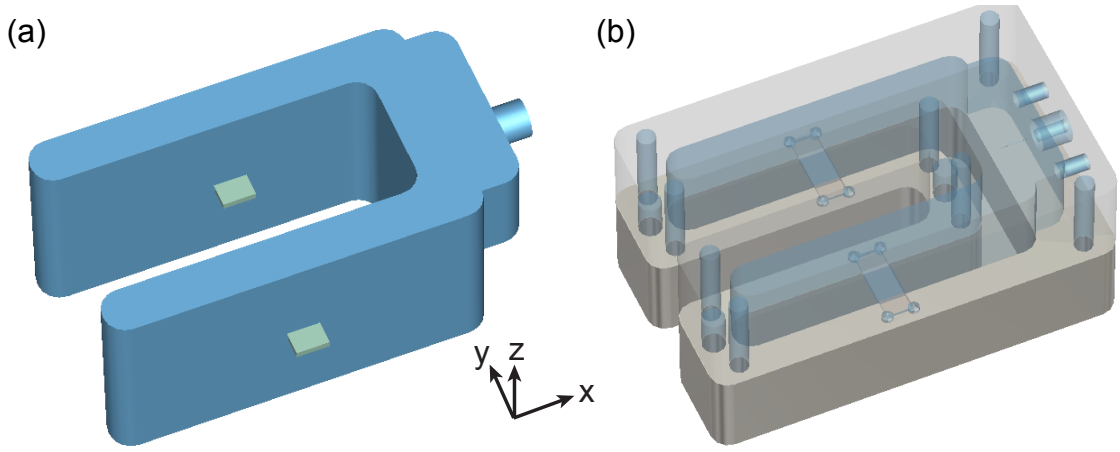

Figure 3.1: (a) CST cavity model. The blue vacuum is surrounded by PEC (not visible). Silicon chips are depicted in green. (b) CST cavity model of imported CAD cavity drawing. Vacuum is depicted in blue and PEC in grey.

3.2.1 Horseshoe cavity design

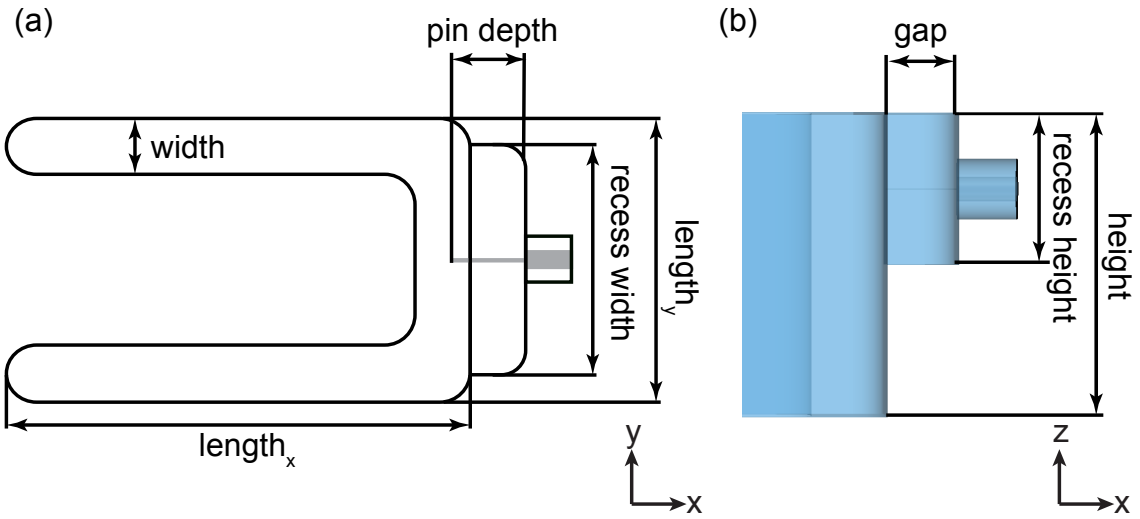

Figure 3.2: Cavity design parameters. (a) Relevant design parameters of a cross section through the antenna plane. The antenna is depicted in grey. (b) Xz-profile of the cavity with relevant design parameters. The blue color code indicates vacuum.

In the following, the optimization process of the horseshoe cavity is described. For this task, all relevant design parameters are sketched in Fig. 3.2.
The *width* of the cavity is fixed to 5 mm, so that our standard qubit chip fits in and can be fixed easily. Details on the qubit chip placement can be found in Sec. 3.2.3. The resonance frequency of the cavity mainly depends on its $length_x$, $length_y$ and *height*. CST provides a tool, that optimizes these parameters in predefined ranges to achieve any required eigenfrequency. This is done by starting the frequency solver and setting the target frequency to be the one with minimum reflection in the optimizer. For the final cavity design in this thesis the following parameters are used: $length_x = 40\,\text{mm}$, $length_y = 24.5\,\text{mm}$ and $height = 20\,\text{mm}$.
To achieve a cavity design that provides an overcoupled readout mode and, simultaneously, an undercoupled storage mode, *gap*, *pin depth*, *recess width* and *recess height* are optimized. For this task, the optimizer of the eigenmode solver is used and the following optimization goals are defined:

- $Q_\text{x}^\text{RO} < 1000$
- $Q_\text{x}^\text{S} > 10^{15}$
- $Q_\text{x}^\text{S}/Q_\text{x}^\text{RO} > 10^{14}$.

The parameters *gap* and *pin depth* are finally optimized to 4.73 mm, *recess width* to 20 mm and *recess height* to 9.33 mm. As this value for the *recess height* is more difficult to build by the workshop, it is set to 10 mm, which does not make a major difference in the Q-factor performance.
In order to prevent the development of high electric fields due to sharp corners, edges are rounded. With the help of a parametric sweep, the optimal radius is determined to be 2.3 mm.

3.2.2 Horseshoe mode structure

The electric field distribution of the different cavity modes is simulated with the CST eigenmode solver and depicted in Fig. 3.3 for the first 16 modes. For the first mode [cf. Fig. 3.3 (a)], the electric field mainly lives in the recess of the cavity and runs parallel to the connected dipole antenna. Thus, according to Eq. (2.5), it couples strongly to the antenna resulting in a low external Q-factor which is appropriate for a readout mode. For the final cavity model from Fig. 3.1 (b), the simulated external Q-factor is given by $Q_\text{x}^\text{RO} = 1105.90$.
In contrast, for the second mode [cf. Fig. 3.3 (b)], the electric field mainly lives in the

arms of the horseshoe geometry. At the antenna position, there is nearly no field, so the external Q-factor of this mode is very high which is suitable for a storage mode. For the final cavity design from Fig. 3.1 (b), the simulated external Q-factor is $Q_{\mathrm{x}}^{\mathrm{S}} = 2.18 \cdot 10^{12}$.

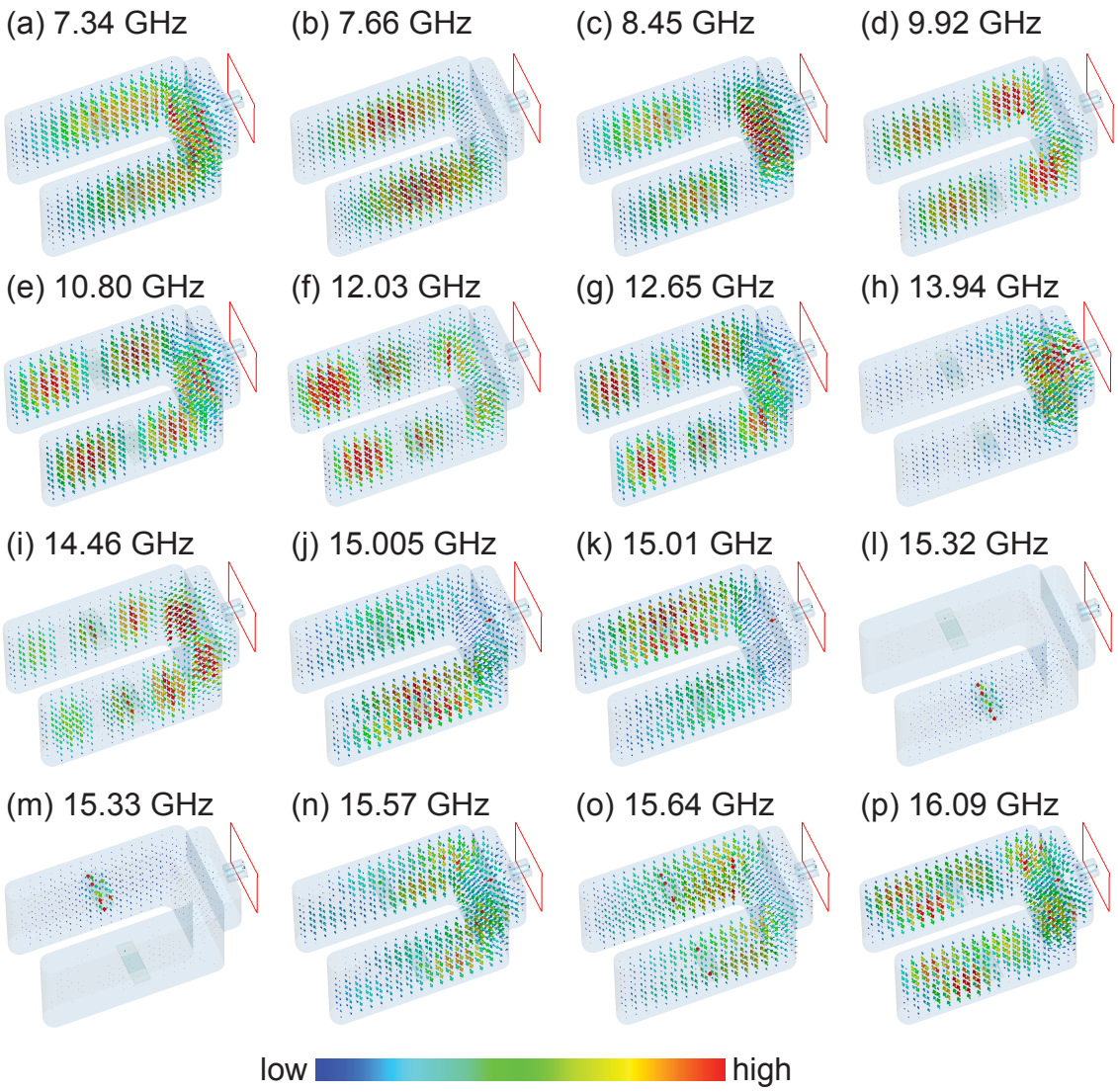

Figure 3.3: Simulated electric field distribution of the first 16 cavity modes for a cavity including two silicon chips. Results for the material silicon lossy and loss free do not make a difference in this case. The red rectangle marks the input and output port. The color code shows the field magnitude in arbitrary units.

One advantage of this horseshoe design is the frequency gap between the storage mode in Fig. 3.3 (b) and the next higher mode in Fig. 3.3 (c). With 790 MHz, it is

more than 17 times larger than the one for the rectangular cavity design [14] and thus it is unlikely that the next higher mode is excited unintentionally.

3.2.3 Chip placement

To guarantee for a symmetric field distribution, the horseshoe cavity includes two silicon chips of size $3.5 \times 10 \times 0.525\,\mathrm{mm}^3$ which either contain a qubit or serve as dummy chips.
The chips should be positioned in such a way that the qubits couple to both readout and storage mode. Thus the electric field component in parallel to the qubits, which in this thesis is the y-component, should be as high as possible. On the other hand internal losses caused by the insertion of the chips should be minimized. As high electric fields at the chip position lead to higher dielectric losses and thus lower internal Q-factors, a comprise regarding the chip placement has to be found.

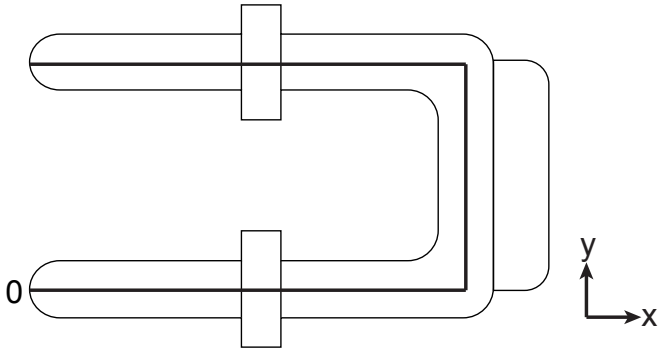

Figure 3.4: Cavity cut through the chip plane. In the simulation, the y-component of the electric field is evaluated along the black curve with origin 0.

To examine the y-component of the electric field along the curve depicted in Fig. 3.4, CST provides the "Evaluate Field on Curve" tool as a postprocessing step in the eigenmode solver. The electric field is distributed symmetrically with respect to the arms of the cavity, so when in the following a position of the first arm is discussed, the same results apply to the opposite position of the second arm.
To get an impression of the electric field for the different cavity modes, simulation results for a cavity model without the chips are plotted in Fig. 3.5 (a). Here the maximum E_y-field for the storage mode is reached at a curve position of 24 mm. The maximum of the readout mode at 32 mm is also the position, where storage mode and readout mode have the same E_y. An advantage of the cavity design is that the next higher mode has its maximum at 16 mm and drops constantly for

higher positions. So the chips could be easily positioned in a way that they couple strongly to readout and storage mode, while minimizing the coupling to the next higher mode.

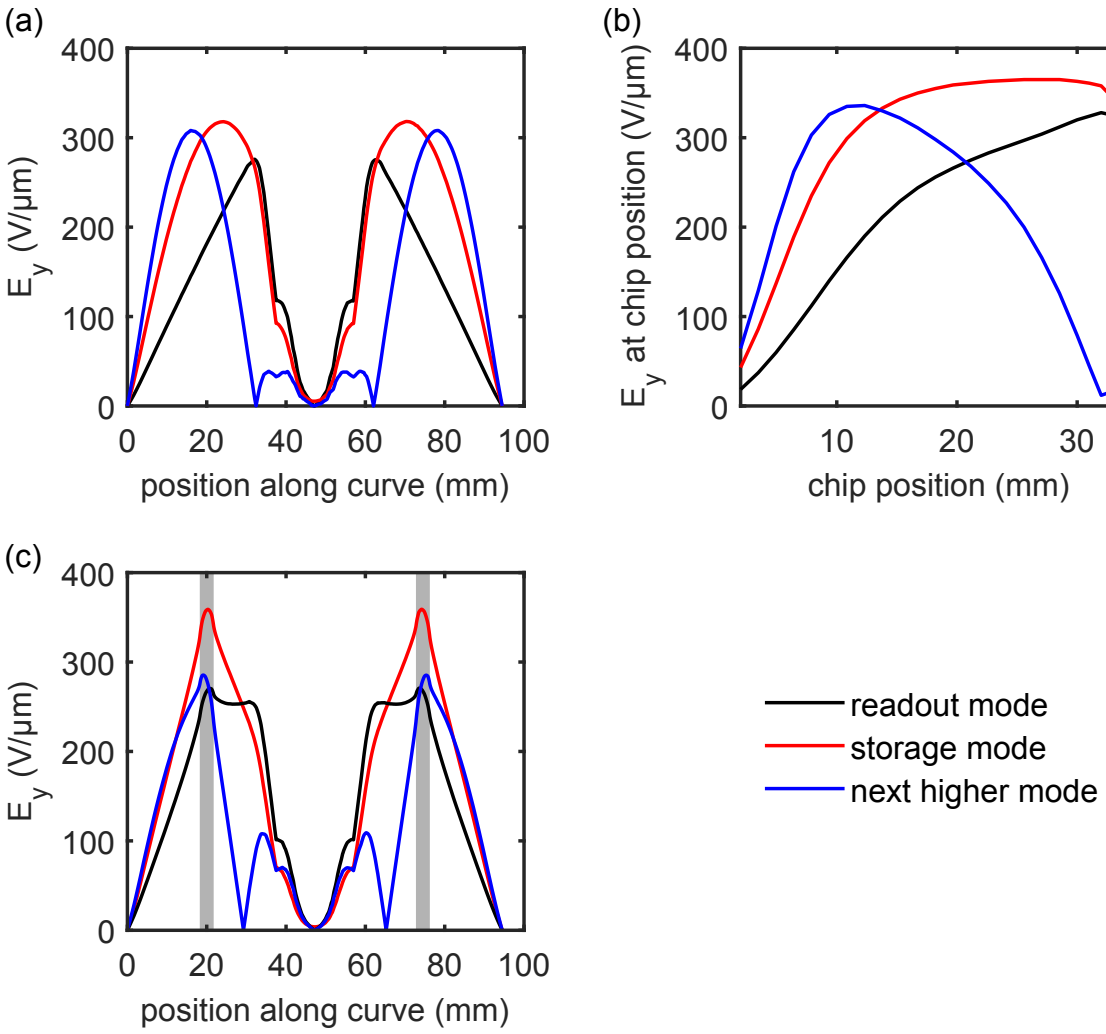

Figure 3.5: (a) and (c) Simulated y-component of the electric field evaluated along the curve depicted in Fig. 3.4. In (a) the simulation model does not include the chips while in (c) the chip areas are marked in grey. (b) Simulated y-component of the electric field evaluated at the center of the chip position for different chip center positions.

As the insertion of a dielectric affects the electric field distribution, a simulation including the chips has to be performed. A parametric sweep allows to evaluate the electric field along the curve for different chip positions. Here "position" refers to the distance between curve origin and chip center. Figure 3.5 (b) plots the E_y-field at the chip center for different chip positions. The storage mode is not very sensi-

tive to different chip positions: The maximum E_y-field is reached for a chip position at 27 mm, still maintaining 98 % at 20 mm and 32 mm. The readout mode has a maximum at 32 mm, constantly dropping to 92 % at 27 mm and 82 % at 20 mm. An equal coupling constant for readout and storage mode can be reached for a chip position at 35 mm, where the storage mode has dropped to 74 % and the readout mode to 83 % of their maximum E_y-field. The next higher mode has its maximum at 11 mm, constantly dropping for higher chip positions. At 21 mm the next higher mode crosses the readout mode and reaches its minimum at 32 mm with only 4 % of the readout mode E_y-field. So if the main criterion for an appropriate chip placement consisted in reaching a maximal E_y-field for readout and storage mode while maintaining a vanishing E_y-field for the next higher mode, a chip position between 27 mm and 32 mm would be chosen.

The second criterion which has to be taken into account when placing the chips are dielectric losses and corresponding internal Q-factors. For this simulation, the cavity model has to include the cavity casing consisting of PEC. Dimensions of the cavity casing (cf. App. B) do not affect the inner cavity performance, so they are chosen to be as small as possible in order to cool down fast and save space inside the measurement cryostat.

With the help of the "Loss and Q Value from H-Field" tool, dielectric losses and internal Q-factors can be evaluated. Here, CST uses the expression "TotalQ" instead of internal Q-factor. When choosing "silicon loss free" as the chip material, the internal Q-factor only includes surface losses and largely does not depend on the chip position. For chip positions from 15 mm to 32 mm, the internal Q-factors of readout and storage mode are simulated to $Q_0^{\mathrm{RO}} = (1.03\text{–}1.04) \cdot 10^6$ and $Q_0^{\mathrm{S}} = (1.09\text{–}1.10) \cdot 10^6$. When choosing "silicon lossy" as the chip material, dielectric losses are considered in the Q-factor calculation yielding lower internal Q-factors at higher E_y-fields. So at 32 mm, where the E_y-field of the readout mode is highest, the internal Q-factor of the readout mode is simulated to $Q_0^{\mathrm{RO}} = 3.39 \cdot 10^5$, which is the lowest value. For lower chip positions the internal Q-factor of the readout mode is constantly rising, reaching $Q_0^{\mathrm{RO}} = 4.04 \cdot 10^5$ at 20 mm. The lowest internal Q-factor of the storage mode is simulated to $Q_0^{\mathrm{S}} = 3.03 \cdot 10^5$ at 27 mm, where the E_y-field of the storage mode is highest. At 32 mm, where the E_y-field is decreasing again, an internal Q-factor of $Q_0^{\mathrm{S}} = 3.11 \cdot 10^5$ and, at 20 mm, an internal Q-factor of $Q_0^{\mathrm{S}} = 3.09 \cdot 10^5$ is simulated.

In this thesis, a chip position of 20 mm is chosen as a compromise between high E_y-field of readout and storage mode and high internal Q-factor, although the E_y-field of the next higher mode at this chip position is the same order of magnitude as that

of the readout mode. Electric field simulation results for this model are plotted in Fig. 3.5 (c). As the resonance frequency of the next higher mode is 790 MHz detuned from the storage mode, we assume that the next higher mode is not excited and therefore the rather high E_y-field at the qubit position is not a problem.

Since the transmon qubit is both finite in size and possibly not exactly in the middle of the chip, the electric field at the wall–chip interface should be maximally reduced by a factor of two with respect to the electric field in the middle of the qubit chip. The relevant quantity in this case is the y-component of the electric field because it is responsible for the mode–qubit coupling. Simulation results in Fig. 3.6 show that the y-component of the electric field at the borders of the qubit chip is still 77 % compared to the center of the chip, which is still sufficient for the mode–qubit coupling.

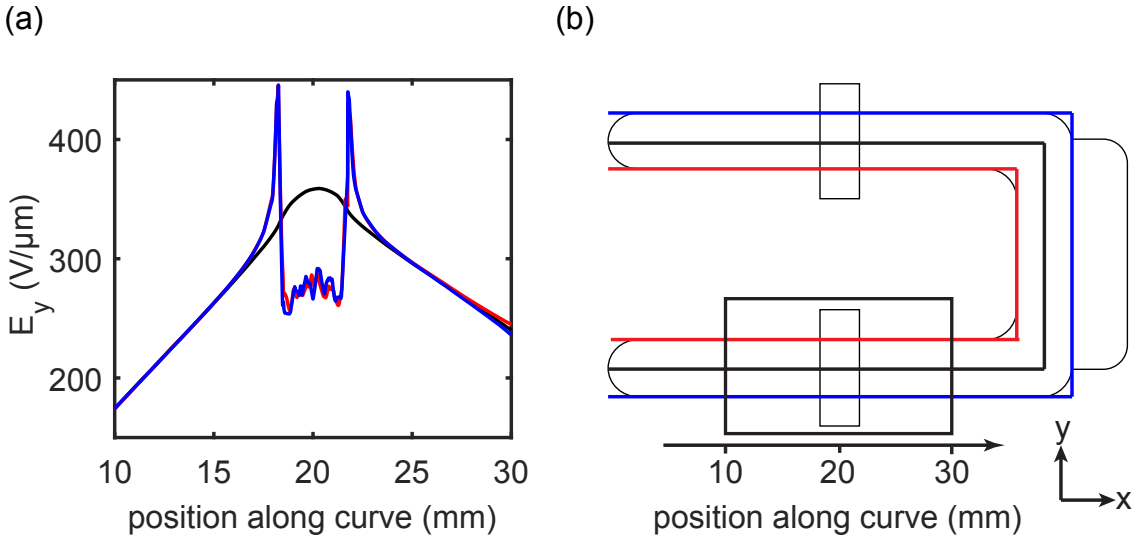

Figure 3.6: (a) Simulated y-component of the electric field of the storage mode along the curves modeled in (b). The curves lie in the qubit-chip plane, evaluating the electric field in the middle of the chip (black) and at the wall–chip interface (red, blue). The black box marks the range of examined chip positions in (a).

An interesting effect arises at the edges of the cavity–chip interface: Due to the sharp corners, there is a discontinuity in the E_y-field strength. Here the E_y-field is about 20 % higher than in the middle of the chip. To have a closer insight into the discontinuity, Fig. 3.7 evaluates the E_y-field along the cavity–chip interface and

in comparison to that along two curves shifted to the left and to the right. For all three curves, the E_y-field stays constant from approximately 0.5 mm away from the cavity wall. The discontinuity, which arises inside these 0.5 mm has no direct effect on the qubit in the middle of the chip. However other two-level systems, which for instance arise from defects inside the silicon chip, can be excited and can contribute to a faster decoherence of the qubit. Nevertheless, in this thesis it is assumed that qubit coherence times are not limited by the discontinuity. For future designs, one could consider modifying the shape of the horseshoe to prevent such discontinuities.

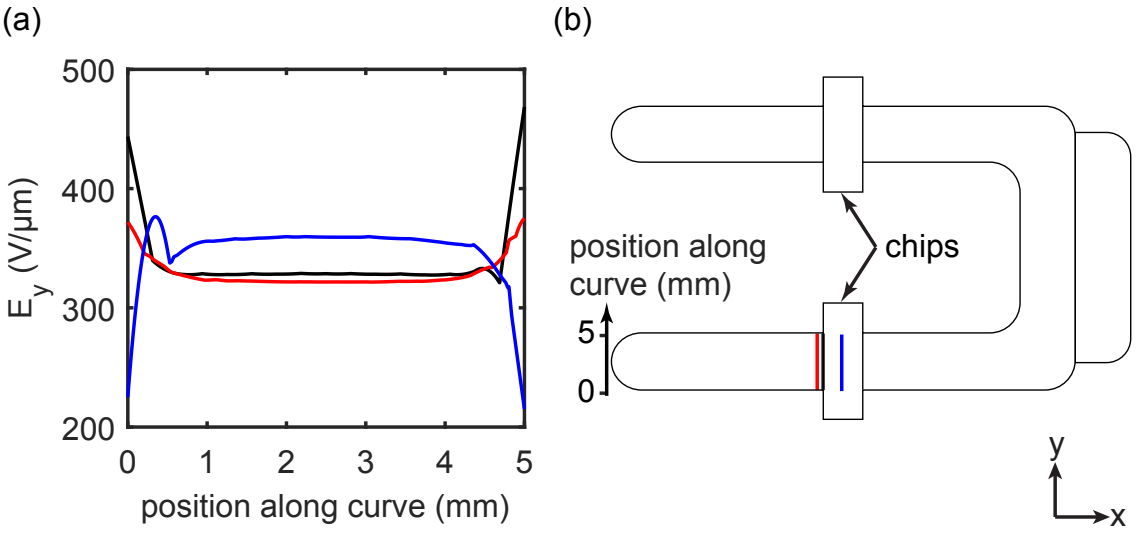

Figure 3.7: Simulated y-component of the electric field of the storage mode along the curves modeled in (b). The curves lie in the qubit-chip plane, evaluating the electric field at the cavity–chip interface (black), 0.25 mm to the left of the discontinuity (red) and in the middle of the chip (blue).

3.2.4 Antenna design

Serving as input and output port, the used dipole antenna is the source for external losses (see Sec. 2.1.2). Therefore it is important to examine the electric field strength parallel to the antenna for readout, storage and next higher mode of the cavity. This is done by modeling a line along the antenna's position with CST [cf. Fig. 3.8 (b)] and using the "Evaluate Field on Curve" tool as a postprocessing step in the eigenmode solver. The result of the simulation is plotted in Fig. 3.8 (a), showing that there is a factor of 1000 between the electric field strength of readout and storage mode. As the external loss rate κ_x is proportional to the square of the electric field strength [see Eq. (2.5)], the external loss rate of the readout mode is a factor of a million higher

than that of the storage mode. So the main requirement of a compact quantum memory providing a maximal coupling of the readout mode while maintaining a minimal coupling of the storage mode is fulfilled.

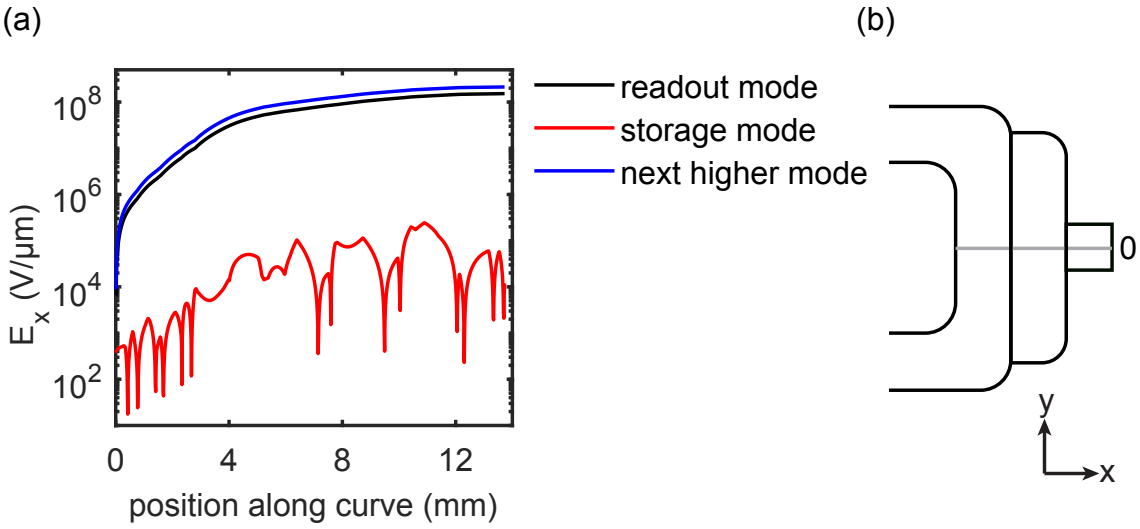

Figure 3.8: (a) Simulated electric field strength along a line parallel to the antenna for readout, storage and next higher mode. (b) Line parallel to the antenna (grey) with origin at 0.

As in reality the antenna can never be placed with perfect accuracy, it is important to investigate how sensitive the Q-factor performance is to a displacement or tilt. Furthermore, it has to be verified that the asymmetric antenna position in z-direction does not influence a symmetric field distribution around the qubit chip plane.
As a last part of the antenna design, the fixation of the antenna to the cavity has to be discussed.

Impact of a displaced antenna

In Fig. 3.9 (a), the external Q-factor of the storage mode is simulated for different y-positions of the antenna. The model taken for the simulation is depicted in Fig. 3.9 (b). A maximum Q-factor is reached for an antenna position in the middle of the two arms at $y = 0$, where the electric field is oriented in parallel to the antenna and consequently the coupling vanishes. As a slimmer antenna is not as sensitive to a displacement in y-direction, in this thesis we use a 0.1 mm diameter antenna. Details on the antenna fabrication are found in Sec. 4.1.1.
The positioning window for reaching an external Q-factor of 10^6, which is approxi-

mately the order of magnitude of the internal Q-factor, is ±0.53 mm for the 0.1 mm diameter antenna. Thus, if the antenna is displaced by half of a millimeter, the over-coupled regime of the storage mode is reached and the storage time of a qubit state decreases. In comparison to the rectangular cavity design, the positioning window of the horseshoe model increases by a factor of four [14].

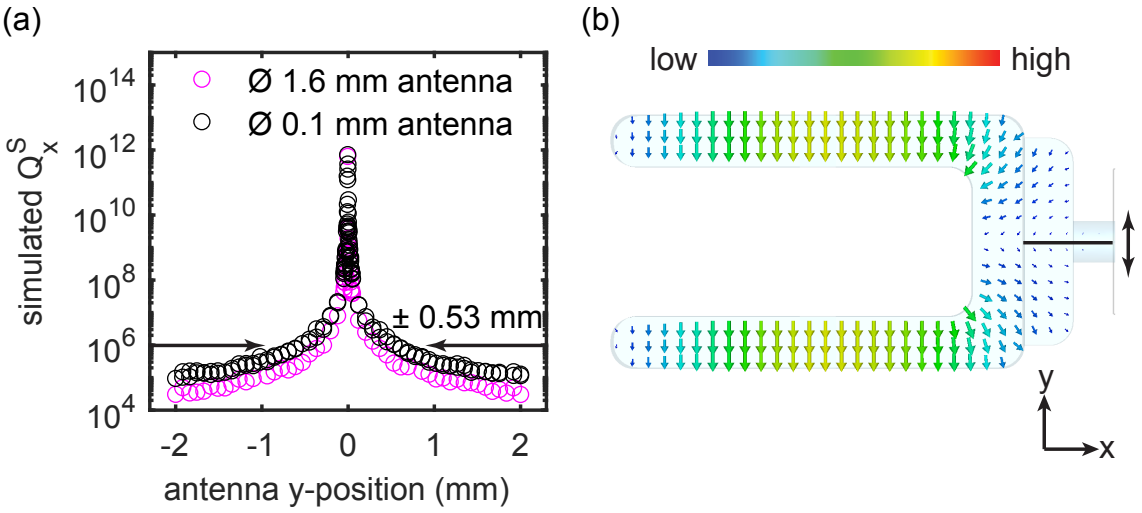

Figure 3.9: (a) Simulated external Q-factor of the storage mode depicted as a function of the antenna y-position for two different antenna diameters. (b) Simulated electric field distribution on a cross section through the antenna plane for a centered antenna position. The color code shows the field strength in arbitrary units, the arrows indicate the field orientation. The solid black line is the 0.1 mm diameter antenna.

Impact of a tilted antenna

Another factor which leads to a Q-factor reduction is a tilted antenna. As the antenna actually consists of a thin gold wire soldered onto a commercial antenna, it may not be perfectly straight. More details on the antenna fabrication can be found in Sec. 4.1.1. The influence of such a tilt in the xy-plane is simulated in Fig. 3.10. For a slightly displaced antenna, even a tilt of 10° does not have a major influence.

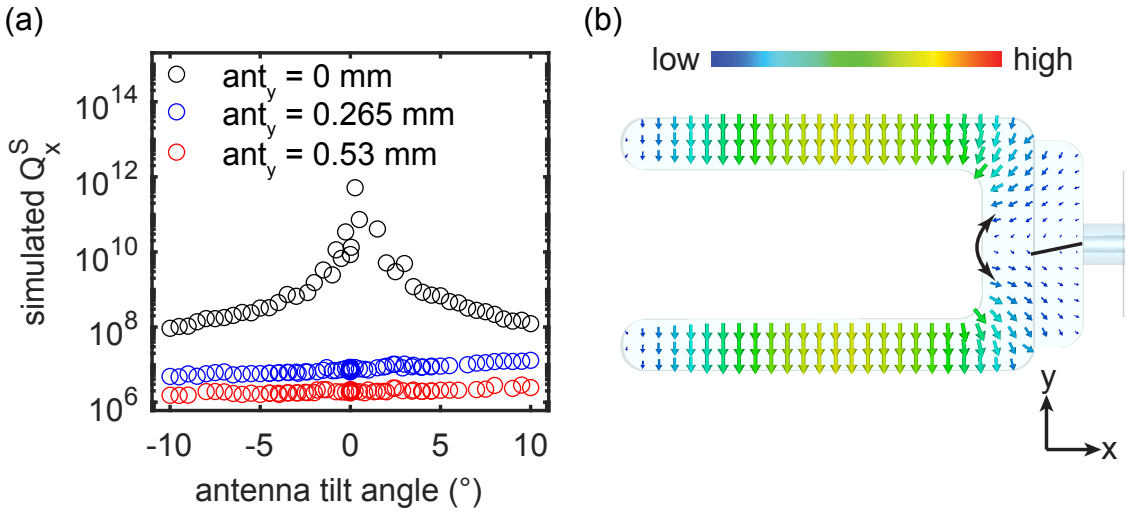

Figure 3.10: (a) Simulated external Q-factor of the storage mode depicted as a function of the antenna tilt angle. Simulation results are shown for a perfectly positioned antenna (black) and for an antenna displaced in y-direction by 0.265 mm (blue) and 0.53 mm (red). (b) Simulated electric field distribution on a cross section through the antenna plane for a centered antenna position and an antenna tilt angle of 10°. The color code shows the field strength in arbitrary units, the arrows indicate the field orientation. The solid black line is the tilted 0.1 mm diameter antenna soldered onto a commercial antenna which is depicted in blue.

Impact of asymmetric antenna position in z-direction

To place the qubit chips inside the cavity volume, the cavity has to be fabricated in two halves. The antenna is designed to be screwed to the middle of the recess of the upper cavity half. Thus the antenna is positioned asymmetrically with respect to the z-direction of the cavity. To justify this design, it has to be shown that a symmetric field distribution around the qubit chip plane is guaranteed. As the y-component of the electric field couples to the transmon qubit, this is the relevant quantity to be simulated for different z-positions. Simulation results are shown in Fig. 3.11. Near the qubit chip position the electric field is distributed symmetrically in positive and negative z-direction. A maximum is reached at the qubit chip position. Two millimeters above and below the qubit there are still 87 % and four millimeters above and below the qubit there are still 71 % of the maximum electric field strength. Only in the recess near the antenna's position there is a slight deviation in the electric field

strength above and below the qubit chip plane, which is illustrated in Fig. 3.11 (c). But as the field is distributed symmetrically around the qubit chips, where it could influence the performance of the qubit–mode coupling, the presented design of the antenna is appropriate for the quantum memory.

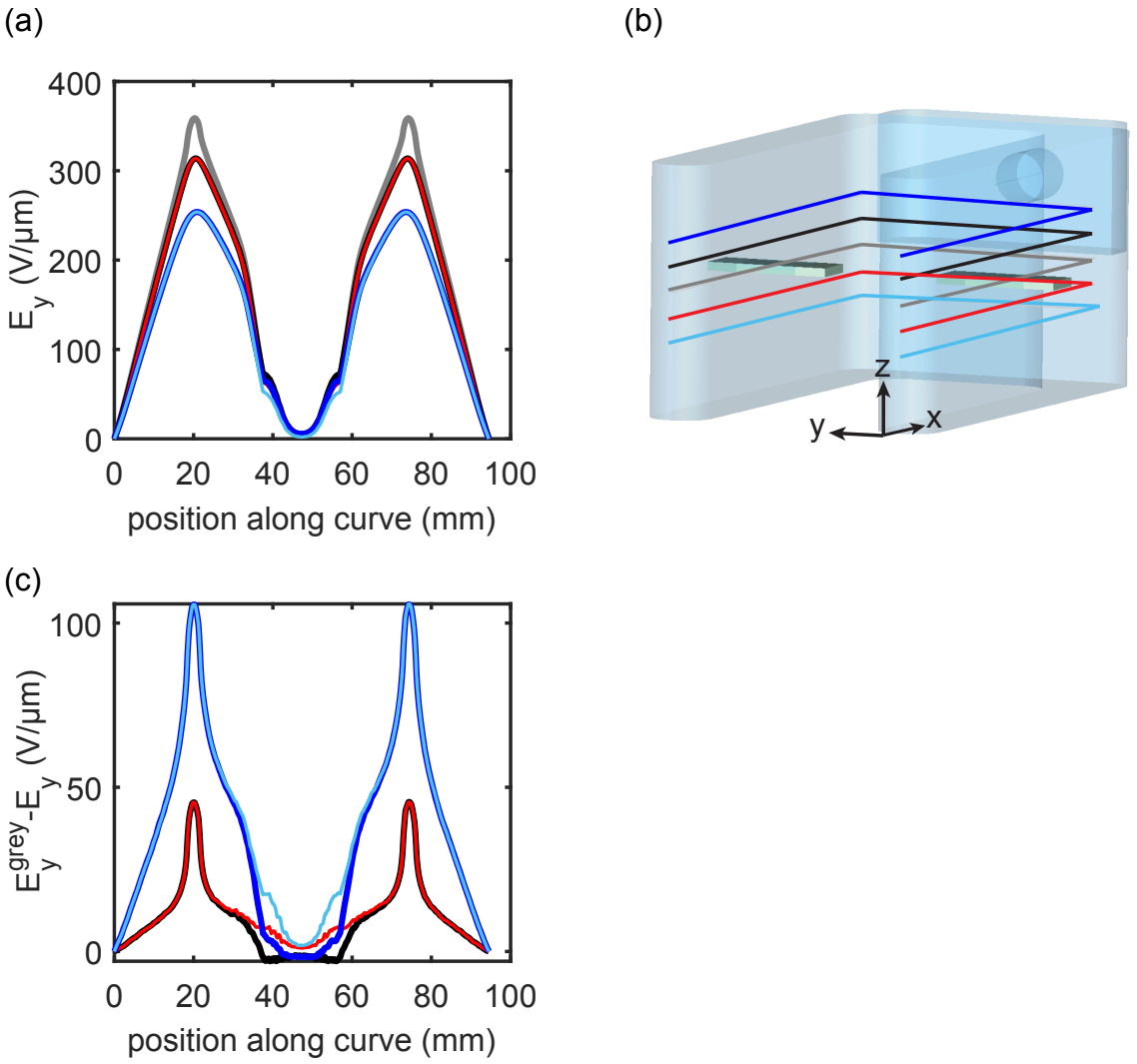

Figure 3.11: (a) Simulated y-component of the electric field strength of the storage mode along the curves indicated in (b). (b) Curves along which the electric field is evaluated. The grey curve lies in the qubit chip plane. Black and red curves are shifted by 2 mm in positive respectively negative z-direction. Dark blue and light blue curves are shifted by 4 mm in positive respectively negative z-direction. (c) Simulated E_y-field deviation of the other curves (black, red, dark blue and light blue) from the grey curve.

Antenna fixation

The final antenna has to be attached to the cavity with two screws. In the work of E. Xie [14], the corresponding cavity wall is designed to be thick enough to allow for blind holes. Hence, the presence of the holes does not affect the performance of the cavity.
As the cavity is cooled down to millikelvin temperatures and aluminum is a bad thermal conductor the aluminum walls of the cavity should be as thin as possible. This demand motivates to examine the impact of two additional holes drilled through the cavity wall for antenna fixation.

Table 3.1: CST simulation results are shown for cavity designs where the two holes for the antenna fixation are not drilled through (no holes) or drilled through. For the second case, the impact of screws reaching 3 mm inside the cavity and made of different materials is examined. The model taken for the simulation includes chips made of "silicon lossy".

	no holes	vacuum	brass screws	plastic screws	PEC screws
Surface Losses RO mode (Loss/W)	$4.41 \cdot 10^4$	$4.31 \cdot 10^4$	$9.11 \cdot 10^1$	1.12	6.10
Surface Losses S mode (Loss/W)	$4.40 \cdot 10^4$	$4.31 \cdot 10^4$	$1.00 \cdot 10^1$	$8.22 \cdot 10^{-2}$	$6.68 \cdot 10^{-1}$
Q_0^{RO}	$1.85 \cdot 10^5$	$1.91 \cdot 10^5$	$2.32 \cdot 10^5$	$2.32 \cdot 10^5$	$2.32 \cdot 10^5$
Q_0^{S}	$1.16 \cdot 10^5$	$1.18 \cdot 10^5$	$1.32 \cdot 10^5$	$1.32 \cdot 10^5$	$1.32 \cdot 10^5$
$Q_{\mathrm{x}}^{\mathrm{RO}}$	1703.27	930.75	1106.03	1105.90	1106.94
$Q_{\mathrm{x}}^{\mathrm{S}}$	$1.38 \cdot 10^{12}$	$7.14 \cdot 10^{12}$	$1.18 \cdot 10^{12}$	$2.18 \cdot 10^{12}$	$1.86 \cdot 10^{12}$

As the electric field decays exponentially inside an aperture [14] the additional holes are not expected to have a crucial impact on the external Q-factors. The internal Q-factors are also expected to stay constant or even rise a bit because of lower surface losses. Simulation results which are summarized in Tab. 3.1 confirm that the influence of the additional holes can be neglected. The comparison of different screw materials shows that plastic screws have the best performance. The external Q-factor of the storage mode is highest and of the readout mode lowest.

So the antenna screws used in this thesis consist of a plastic called polyether ether ketone (PEEK) and are produced by the workshop at WMI.

3.2.5 Scalability

Considering DiVincenzo's requirements for the implementation of quantum computing [19], a quantum memory should be designed in such a way that there is the possibility to increase the number of qubits. This can be accomplished very easily by interleaving horseshoe cavities as shown in Fig. 3.12, where the cavities can be scaled along the y- and z-direction while the control access is addressed in x-direction. The distance between neighboring arms is 1.5 mm, which is small enough to use bridge qubits. A bridge qubit is a qubit which couples to two arms and is implemented on a chip connecting these arms. Furthermore, it is possible to shift the cavities in height and build a whole block of memory cells while being able to control each of the cells separately.
For multiplexed readout, the resonance frequencies of the cavities have to differ from each other. This can be accomplished by integrating different dampers in each cavity. For instance an aluminum block replacing a small part of the vacuum might serve as a damper. The advantage of this approach is that each cavity has a different resonant frequency while the geometric design is the same. Another option would be to use different geometries that fit together.

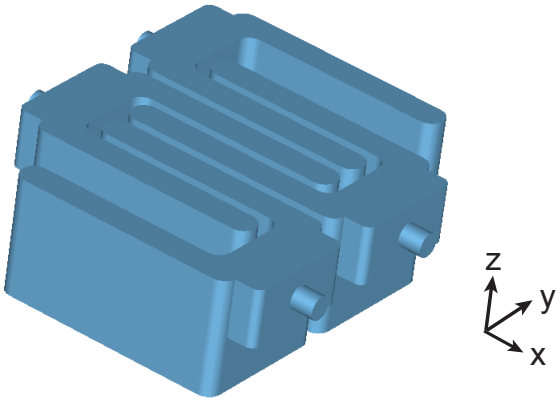

Figure 3.12: Design of a horseshoe chain. The distance between neighboring arms is 1.5 mm which is small enough to use bridge qubits.

Chapter 4

Experimental techniques

4.1 Sample design

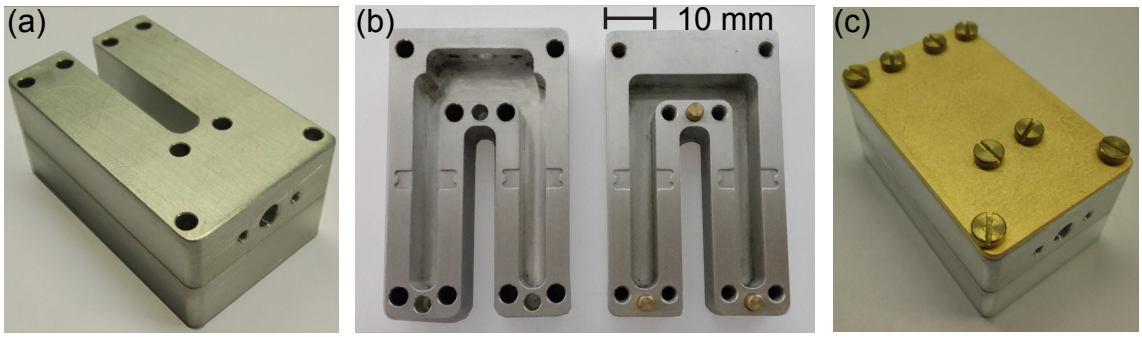

Figure 4.1: Photograph of the final horseshoe cavity built by the workshop at WMI. (a) Closed cavity. (b) Cavity halves. The upper cavity half on the left contains the recess and the antenna port. (c) An approximately 1.5 mm thick gold-plated copper plate is screwed onto the cavity for better thermal conductance.

After completing the design and optimization of the horseshoe cavity as discussed in Chapter 3, the final cavity model is built by the workshop at WMI. A detailed CAD drawing of the model can be found in App. B.

Figure 4.1 (a) shows a photograph of the resulting horseshoe cavity. To guarantee for an accurate positioning of the two cavity halves depicted in Fig. 4.1 (b), they are bolted with the help of three dowel pins.

As the cavity is made of aluminum, which has a weak thermal conductance in the superconducting state, it takes long to cool it down. Therefore, besides minimizing the wall thickness, an approximately 1.5 mm thick gold-plated copper plate is screwed onto it and thermally connected to the sample rod by two annealed silver wires.

This plate is depicted in Fig. 4.1 (c). Before gold-plating the plate galvanically, it is annealed at 850 °C for one hour and then cooled down to room temperature slowly to even increase the conductance.

4.1.1 Coupling antenna

The horseshoe cavity is designed to have only one antenna simultaneously serving as an input and output port to perform reflection measurements. As discussed in Sec. 3.2.4, a slimmer antenna allows for more position inaccuracy. Therefore a 0.1 mm diameter gold wire is soldered onto a commercial 1.6 mm diameter antenna[1]. The exact process is described in the following:
First, the commercial antenna is shortened to a length of 4 mm. Then, a hole with a diameter of 0.15 mm and a depth of approximately 1 mm is drilled in the center of the connector end. As a next step, the antenna is cleaned with an ultrasonic bath first in a beaker filled with acetone for one minute and second in a beaker filled with isopropanol for 30 seconds. For soldering the gold wire inside the drilled hole the antenna is fixed under a tabletop stereo microscope. Then, one end of the gold wire is dipped into Castolin[2] before it is stuck into the drilled hole and soldered. Figure 4.2 (a) shows how the gold wire is finally cut to the correct length of 4.7 mm: The connector end and the end of the gold wire are fixed and the gold wire is cut with the help of a slide gauge. The final antenna screwed to the cavity is depicted in Fig. 4.2 (b).

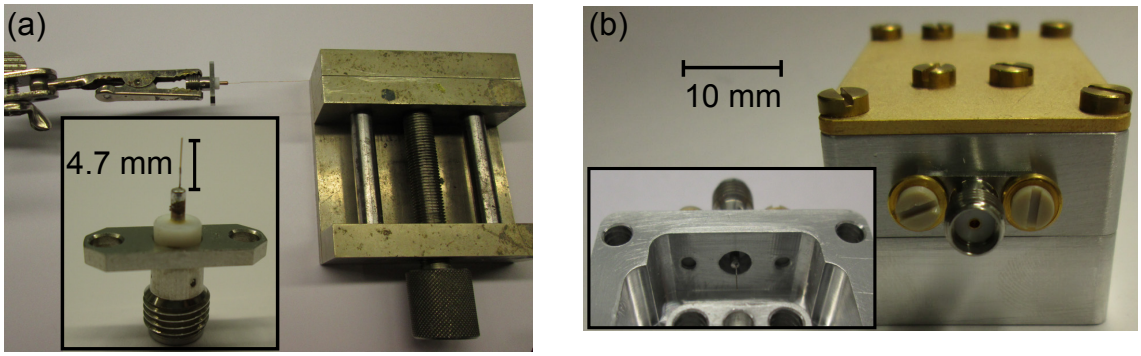

Figure 4.2: (a) Setup to cut the antenna gold wire to the correct length. (b) Photograph of the antenna screwed to the cavity.

[1] Rosenberger SMA 32S722-500S5
[2] Castolin GmbH www.castolin.com

4.1.2 Transmon qubit chips

The first test of the qubit–cavity system is intentionally done with the horseshoe cavity containing two qubit chips. In case one qubit is broken, there would be still the second one to measure. The two transmon qubits QMv3 2nd and C2 used in this thesis are fabricated by Edwar Xie within the scope of his PhD thesis. Details on the fabrication process can be found in Ref. [14].
The silicon chips containing the qubits are placed between the two cavity halves inside the allocated dents and fixed with indium as depicted in Fig. 4.3 (a). An optical micrograph of the qubit QMv3 2nd is shown in Fig. 4.3 (b).

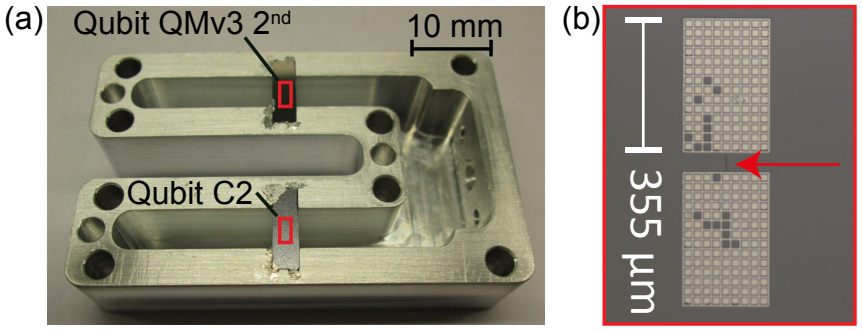

Figure 4.3: (a) Upper cavity half with transmon qubits. The chips containing the qubits are placed inside the allocated dents and fixed with indium. The red rectangles mark the qubit positions. (b) Optical micrograph of qubit QMv3 2nd. The Josephson junction connecting the two capacitor plates is indicated with the red arrow.

4.2 Setup

4.2.1 Cryogenic setup

As cavity and qubit are superconducting and the qubit needs to be protected from thermal excitations, measurements have to be performed at millikelvin temperatures. This is achieved by mounting the horseshoe–qubit system to the base plate of a ^{3}He/^{4}He dilution refrigerator. Details concerning the working principle of the dilution refrigerator can be found in Ref. [38].
A photograph of the cavity mounted to the sample rod is depicted in Fig. 4.4 (a). For better thermalization additional silver wires connect cavity and sample rod. Figure 4.4 (b) sketches the different temperature stages of the dilution refrigerator including the input and output lines of the cavity with all microwave components. At

the base temperature stage, both input and output lines are filtered with a low-pass filter[3] to protect the qubit from high frequency noise.

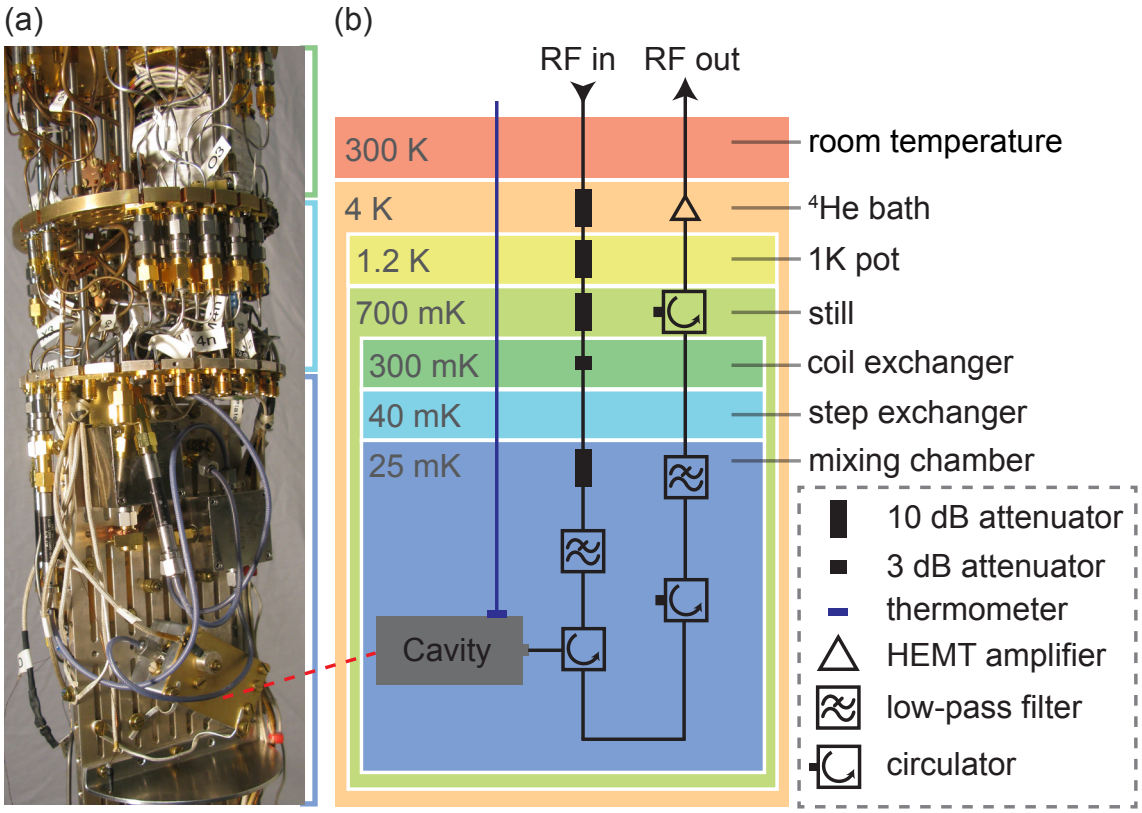

Figure 4.4: Cryogenic setup. (a) Photograph of the base plate of the dilution refrigerator before cooldown. The red dashed line marks the horseshoe cavity. (b) Schematic drawing of the different temperature stages of the cryostat. The input and output line of the horseshoe cavity and all used microwave components are shown.

4.2.2 Frequency domain measurements

The cavity and qubit characteristics are measured in the frequency domain using the setup depicted in Fig. 4.5. For single-tone measurements, a vector network analyzer[4] (VNA) drives the resonator inside the fridge and detects the reflected signal after it passed the cryogenic output setup, a room-temperature isolator[5], and a room-temperature amplifier[6]. In the following, the VNA signal is called readout

[3] K&L 6L-250-12000 tubular filters
[4] Rohde & Schwarz ZVA24
[5] MCLI IS-19-1
[6] AMT-A0019

signal. Two-tone measurements require an additional microwave source[7] to drive the qubit. Readout and qubit drive signals are combined using a power combiner[8] before entering the cryostat.

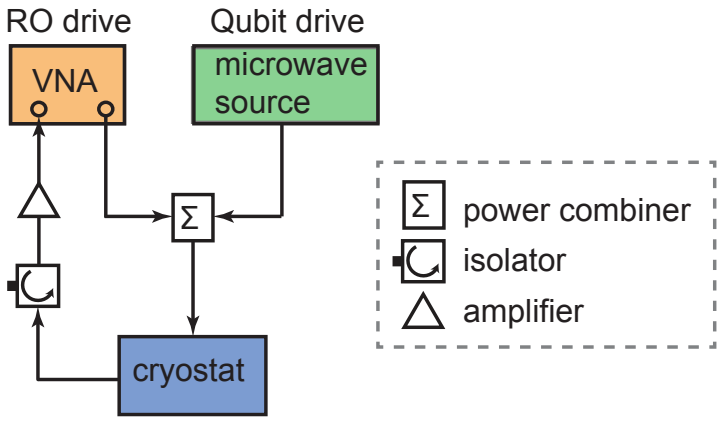

Figure 4.5: Experimental setup for a two-tone measurement. For a single-tone measurement the same setup without the microwave source is used.

4.2.3 Time domain setup

To investigate the dynamics of the qubit–cavity system, a time resolved measurement setup is required [38, 39]. Controlled qubit manipulations can only be achieved with the help of pulsed microwave signals, as the final state of the qubit depends on the pulse length of the drive (see Sec. 2.3.3). To read out the qubit state, the resonator has to be driven right after the qubit pulse. So an accurate sequence timing is needed.

The pulse generation setup used in this thesis is sketched in Fig. 4.6. Usually a microwave source provides a continuous signal at the desired drive frequency and power and an arbitrary function generator[9] (AFG) provides the pulse envelope. The shape of the envelope is chosen to be a flattop Gaussian with a fixed Gaussian ramp of 20 ns on each side. This is advantageous in order to prevent sharp edges and thus a broad frequency spectrum of the pulse envelope, which might excite higher transmon qubit levels [14].

The microwave source responsible for the readout drive[10] is connected to the AFG

[7] Rohde & Schwarz SMF100A
[8] Mini-Circuits ZX10-2-183-S+
[9] Agilent Technologies 81160A
[10] Rohde & Schwarz SMB100A

via two RF mixers[11] in series and a power combiner[12]. The mixers are necessary for a sufficient on/off ratio. The microwave sources used for the qubit drive[13] and BSB drive[14] have a sufficient on/off ratio, so here the mixers are not needed. All drives are finally combined with power combiners[15] before entering the cryostat and eventually the horseshoe cavity.
The postprocessing and analysis of the reflected signal emerging from the horseshoe cavity is done with the help of a field programmable gate array (FPGA) card[16] and a LabView Code on the computer. More details on the measurement setup and recording can be found in Refs. [14, 38, 40].

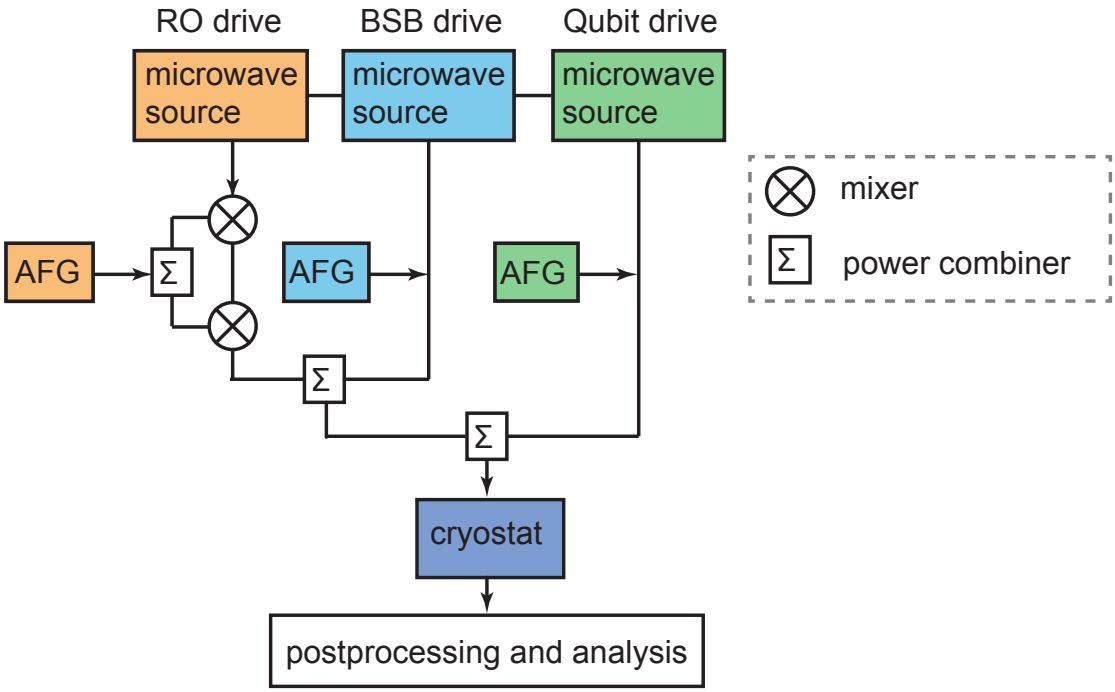

Figure 4.6: Time domain pulse generation setup. A microwave source and an arbitrary function generator (AFG) are each used to generate qubit, BSB and readout pulses with an adjustable power, frequency and pulse length.

[11] Marki M10220LA)
[12] Mini-Circuits ZFRSC-42-S+
[13] Agilent Technologies PSG
[14] Rohde & Schwarz SMF100A
[15] Mini-Circuits ZX10-2-183-S+ and MCLI PS2-11
[16] X5-RX from Innovative Integration

4.3 Spectroscopy

4.3.1 Single-tone measurement

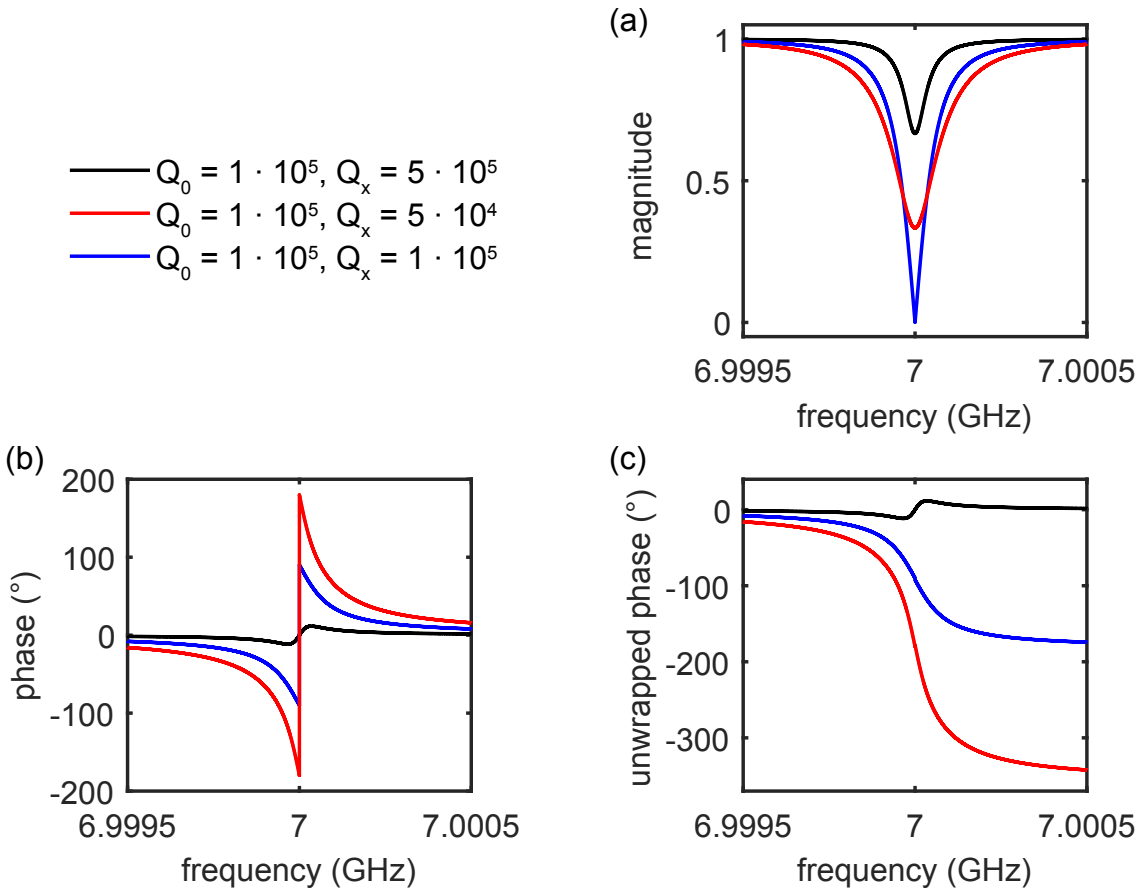

Figure 4.7: Theoretical (a) magnitude, (b) phase and (c) unwrapped phase of the reflection coefficient from Eq. (4.1). The internal Q-factor is kept at $1 \cdot 10^5$, while the external Q-factor is larger (black), lower (red) and equal (blue).

To obtain the resonance frequency of the resonator, a frequency sweep of the readout signal is performed. Whenever necessary, a linear fit line of the measurement data is subtracted to remove background structure.
A simple theoretical model to fit the magnitude and phase of the reflected signal is provided by the input-output formalism which gives the reflection coefficient [41]

$$\Gamma = \frac{\kappa_0 - \kappa_x + 4\pi i(f - f_c)}{\kappa_0 + \kappa_x + 4\pi i(f - f_c)}. \tag{4.1}$$

Here, κ_x and κ_0 denote the external respectively internal coupling rates which determine the external and internal Q-factors according to:

$$Q_{x,0} = \frac{2\pi f_c}{\kappa_{x,0}}. \tag{4.2}$$

The theoretical magnitude and phase of the reflection coefficient are plotted in Fig. 4.7 for different values of the external Q-factor Q_x, respectively a coupling rate κ_x. The phase response is shown in two different ways. Figure 4.7 (b) shows the phase between $-180°$ and $180°$, while Fig. 4.7 (c) shows the unwrapped phase which linearly shifts the angles by multiples of 2π whenever there is a phase jump greater or equal to $180°$.

The resonance frequency of the resonator can be found at the minimum of the reflected magnitude. The size of this minimum is mainly determined by the difference of internal and external Q-factor. For $Q_0 = Q_x$, zero magnitude is reached. A larger $|Q_0 - Q_x|$ leads to smaller dip sizes. The width of the reflection magnitude is proportional to $1/Q_0 + 1/Q_e$, so higher Q-factors lead to narrower dips. In the overcoupled regime, $Q_0 \gg Q_x$, there is a very strong phase response. In the undercoupled regime, $Q_x \gg Q_0$, the phase response is very small.

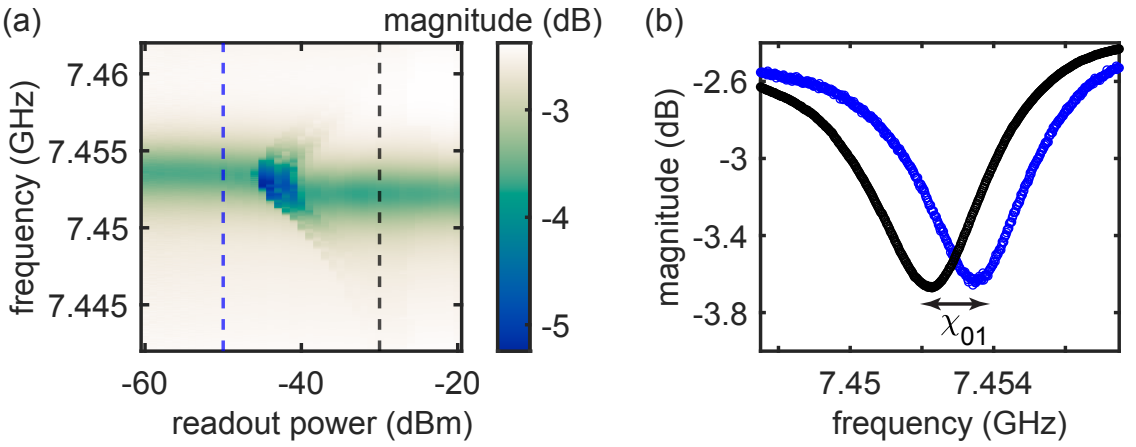

Figure 4.8: Single-tone measurement of the readout mode (horseshoe sample with qubit QMv3 2nd and C2). (a) The reflection magnitude is plotted as a function of drive frequency and power. The blue and black vertical cuts at -50 dBm and -30 dBm, respectively, are shown in (b).

The dispersive shift χ_{01} from Eq. (2.28) can be extracted from a power sweep of the readout signal [40], as shown in Fig. 4.8 (a). At low drive power, the qubit

is in the ground state $|g\rangle$ since the drive is off-resonant from the qubit transition frequency. When a critical power is reached, the qubit decouples from the cavity and the resonance frequency of the cavity shifts towards the bare cavity frequency f_c [42]. To determine this shift, Fig. 4.8 (b) shows two reflection spectra at power values lower and higher than the critical power.

4.3.2 Two-tone measurement and qubit levels

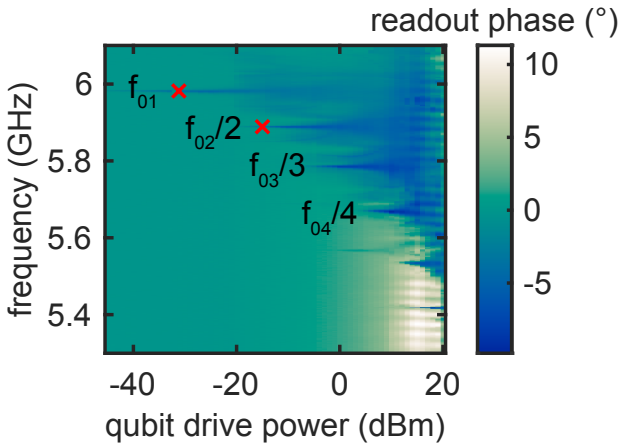

Figure 4.9: Two-tone spectroscopy of the qubit levels. The readout phase is plotted as a function of qubit drive frequency and qubit drive power. The two red crosses mark the transition from the ground state to the first and the second excited state.

The qubit levels are measured using two-tone spectroscopy. Therefore the system is probed with two drive sources (cf. Fig. 4.5): The microwave source is used to drive the qubit while the VNA probes the cavity at its resonance frequency for dispersive readout. If the qubit changes its state, the resonance frequency of the cavity shifts and accordingly a phase shift in the readout signal can be detected. Notice that the power of the cavity probe tone has to be weak enough, that it does not excite the qubit.

In the experiment, the frequency and power of the microwave source are swept. If a qubit transition is induced, a phase shift of the readout signal is detected. Figure 4.9 shows the result of such a measurement. Here, the transition from the ground state to the first excited state already starts at a low drive below one photon on average. We find a qubit frequency $f_{01} = 5.982\,\mathrm{GHz}$. Higher qubit levels are only excited at higher drive powers because of the required multi-photon processes. For instance,

the next transition excites the qubit from the ground to the second excited state in a two-photon process at $f_{02}/2 = 5.889\,\mathrm{GHz}$.
This kind of measurement allows us to calculate the anharmonicity α and the charging energy E_C of the transmon qubit according to Eq. (2.19):

$$\alpha = h(f_{02} - 2f_{01}) \approx -E_\mathrm{C}. \tag{4.3}$$

Further qubit parameters including the total capacitance C_Σ, the Josephson energy E_J and the critical current I_c can be obtained using Eqs. (2.15), (2.17) and (2.14). All qubit parameters are summarized in Tab. 4.1.

4.3.3 AC-Stark shift and photon number calibration

As described in Sec. 2.3.2, the qubit frequency depends on the photon number inside the cavity. To determine the single photon power and obtain the bare qubit frequency, a dispersive readout for different readout powers as depicted in Fig. 4.10 (a) is performed. Here, the qubit drive power of the source is fixed at $-40\,\mathrm{dBm}$ and the qubit drive frequency is swept. The qubit frequency depends linearly on the linearized drive power, as shown in Fig. 4.10 (b). Extrapolating the fit line to zero power determines the bare qubit frequency $f_\mathrm{q} = 5.988\,\mathrm{GHz}$. The single photon power is calculated by plugging in the linear relation:

$$\tilde{\omega_\mathrm{q}} = m \cdot P + \omega_\mathrm{q} \tag{4.4}$$

inside Eq. (2.30) and solving for the power P:

$$P = \frac{2n\chi' + \chi'}{m}. \tag{4.5}$$

With the slope $m = -0.605\,14\,\mathrm{GHz/\mu W}$, a single photon power of $5.9\,\mathrm{nW}$, respectively $-52\,\mathrm{dBm}$ is calculated.
Due to quantum fluctuations about the average photon number inside the resonator, the qubit is affected by random fluctuations in its transition frequency. This phenomenon leads to measurement-induced dephasing resulting in a broader qubit transition dip [28]. The spectroscopic lines of the qubit transitions have a Lorentzian line shape with a FWHM Δf determined by [35]:

$$\pi\Delta f = \sqrt{\frac{1}{T_2^2} + n(2g)^2\frac{T_1}{T_2}}. \tag{4.6}$$

Extrapolating the squared FWHM in Fig. 4.10 (c) to zero power is a rough estimation of the T_2-time:

$$T_2^{\text{est}} = \frac{1}{\pi \Delta f}, \tag{4.7}$$

yielding $T_2^{\text{est}} = (0.47 \pm 0.45)\,\mu\text{s}$. As this kind of measurement procedure sends continuous signals, the influence of measurement-induced dephasing is expected to be bigger than in time domain measurements where the signals are pulsed. Thus, in time domain measurements a slightly longer and more accurate T_2-time is expected.

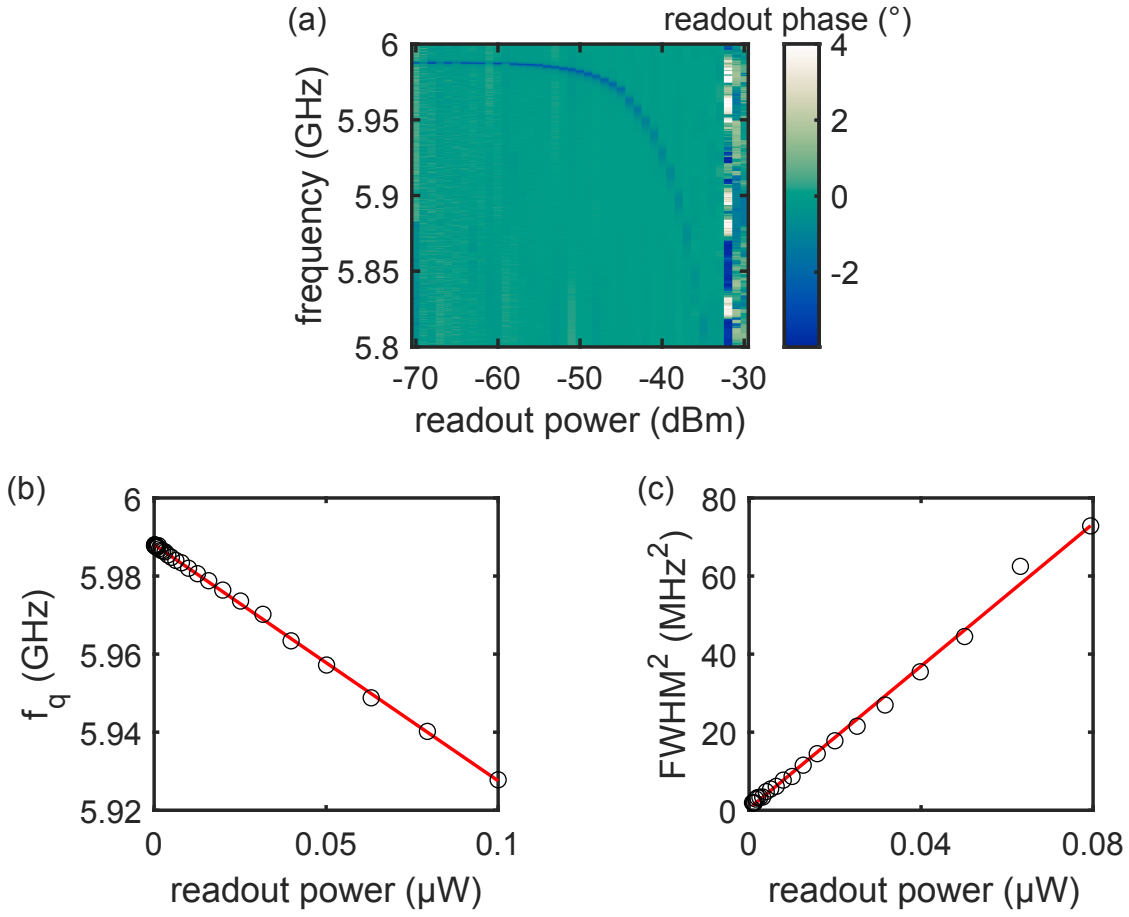

Figure 4.10: (a) AC-Stark shift of the qubit transition frequency depending on the readout power. (b) Photon number calibration. The qubit transition frequency is plotted over the linearized readout power. The red line shows a linear fit to the measurement data. (c) The squared FWHM of the qubit transition is plotted over the linearized readout power. The red line shows a linear fit to the measurement data.

Table 4.1: Summary of qubit parameters determined by spectroscopy.

parameter	Xie 2018	Lamprich 2020
f_q (GHz)	6.234	5.988
α/h (MHz)	-187	-186
C_Σ (fF)	105	104.14
E_J/h (GHz)	26.55	25.57
$E_\mathrm{J}/E_\mathrm{C}$	142	137.46
I_c (nA)	53	51.48

4.4 Time domain measurements

With the help of time domain measurements, qubit and BSB characteristics can be examined in a pulsed manner. Properties such as π- and $\pi/2$-pulse length (see Sec. 2.3.3), energy relaxation time T_1 and decoherence time T_2 (see Sec. 2.4) can be directly extracted from specific pulse protocols. As a final step the implementation of a memory protocol yields the storage time of the qubit state.
All pulse sequences discussed in the following are measured using the time domain setup discussed in Sec. 4.2.3.

4.4.1 Qubit characteristics

The π-pulse length of the qubit can be determined with the help of driven Rabi oscillations. To this end, the qubit is driven at its resonance frequency and the length t of the drive pulse is increased for each sweep. Fitting the measurement data with a damped sine function yields the π-pulse length at the first oscillation dip. As we use flattop Gaussian pulse shapes, the $\pi/2$-pulse length is not exactly half of the π-pulse length. Hence it has to be extracted from a driven Rabi measurement with two identical pulses in series. Here again a damped sine function is fitted to the measurement data and the $\pi/2$-pulse length is half of the time needed for the first oscillation dip. The corresponding pulse schemes for a Rabi with one and a Rabi with two pulses are depicted in Fig. 4.11 (a).
Knowing the qubit π-pulse length allows us to perform an energy relaxation measurement as sketched in Fig. 4.11 (b). The qubit is driven to the excited state and

the time between qubit pulse and readout is increased for each sweep. As a result, the qubit decay due to energy relaxation is recorded and the energy relaxation time T_1 can be extracted.

The decoherence time T_2 of the qubit can be extracted from a Ramsey measurement depicted in Fig. 4.11 (c). With the help of a $\pi/2$-pulse the qubit is excited to the equatorial plane of the Bloch sphere. After a waiting time Δt, which is increased for each sweep, another $\pi/2$-pulse brings the qubit back to the $\hat{z}$-axis and the readout is performed. During the waiting time, the qubit undergoes dephasing and energy relaxation.

A modified version of the Ramsey protocol, which also yields the T_2-time, is given by a spin-echo measurement. Here an additional π-pulse is applied in the middle of the protocol, which cancels the effect of low-frequency noise [38, 43]. The corresponding protocol is depicted in Fig. 4.11 (d).

Typically, the measurement protocols that yield T_1 and T_2-times are repeated several times and the corresponding T_1 and T_2-times are collected in a histogram. This kind of statistics is necessary because energy relaxation and dephasing are statistical processes.

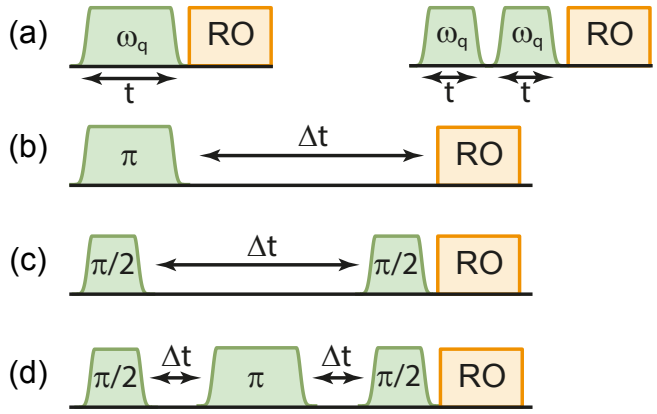

Figure 4.11: Basic pulse protocols to measure the qubit characteristics: (a) driven Rabi oscillations to determine the π- and $\pi/2$-pulse length, (b) relaxation measurement to determine the T_1 decay, (c) Ramsey T_2 measurement, (d) spin echo T_2 measurement.

4.4.2 Blue sideband transition and memory protocol

The storage time of the horseshoe quantum memory designed in this thesis can be measured with a memory protocol. In the following this protocol is discussed by means of the energy spectrum of the coupled qubit–cavity system from Fig. 4.12 (a).

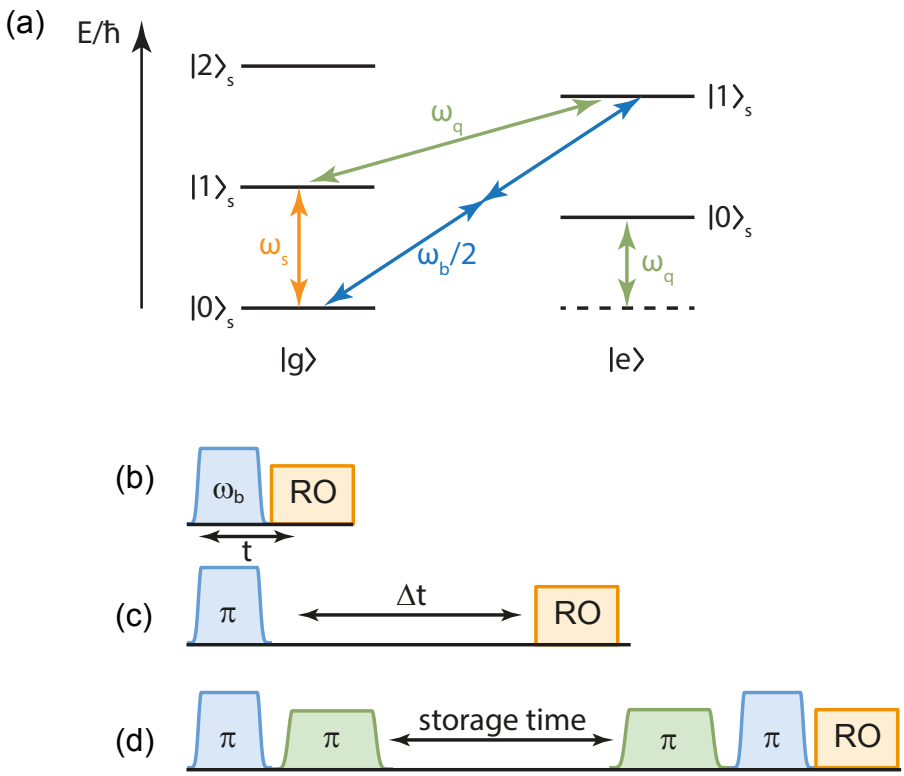

Figure 4.12: (a) Energy spectrum of the qubit coupled to the storage mode of the cavity. The blue arrows indicate the BSB transition which can be driven via a two-photon process. The green arrows indicate qubit transitions, and the orange arrow indicates excitations between the ground and excited state of the storage mode. (b)-(d) Pulse protocols to measure the BSB characteristics and to perform the memory protocol. Blue boxes refer to BSB pulses, green boxes refer to qubit pulses and orange boxes are readout pulses applied to the readout mode. (b) Driven Rabi oscillations to determine the π-pulse length of the BSB transition. (c) Relaxation measurement to determine the T_1 decay of the BSB transition. (d) Quantum memory protocol for storage and retrieval of the qubit state.

There are two different transitions needed for the final protocol: the BSB transition and the qubit transition. Parameters for a qubit transition from $|g1\rangle$ to $|e1\rangle$ and vice versa by a qubit π-pulse are already discussed in the previous section. For the BSB transition from $|g0\rangle$ to $|e1\rangle$, measurements to find the transition frequency and π-pulse length still have to be discussed. The transition frequency can be found by a frequency sweep around the sum of qubit frequency ω_q and eigenfrequency of the cavity's storage mode ω_s. As the BSB transition is a two-photon process, the

drive power has to be substantially higher than for the qubit drive. A dip in the reflected amplitude yields the frequency of the BSB transition $\omega_b/2$. The π-pulse length and the T_1-time of the BSB transitions are extracted from Rabi and relaxation measurements as depicted in Fig. 4.12 (b) and Fig. 4.12 (c).
Knowing all parameters for both qubit and BSB π-pulse allows us to implement the final memory protocol shown in Fig. 4.12 (d). The sequence starts with a BSB π-pulse which excites the ground state population of the qubit to the $|e1\rangle$-state. Then a qubit π-pulse transfers the population to the first excited state of the storage on the left ladder ($|g1\rangle$-state).
For the excited state population of the qubit, the BSB π-pulse has no influence and the qubit π-pulse transfers the population to the ground state of the storage on the left ladder ($|g0\rangle$-state). Consequently, the qubit state is encoded in the first two states of the storage mode [44].
To retrieve the qubit state from the storage, the pulse sequence is implemented in reverse order and a readout is performed. Increasing the storage time for each sweep of the memory protocol records the decay of the stored state and the storage time can be extracted from an exponential fit.

Chapter 5

Results

5.1 Empty horseshoe cavity characterization

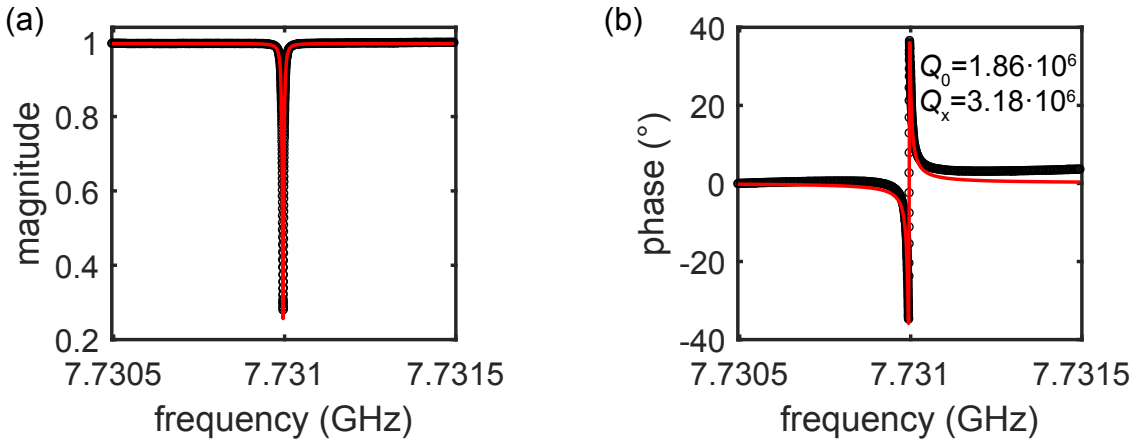

Figure 5.1: Reflection measurement of the undercoupled horseshoe cavity readout mode without chips. Eq. (4.1) is fitted (red line) to the measurement data (black dots). (a) Reflection magnitude. (b) Reflection phase.

This section focuses on the horseshoe cavity without any chips via a single-tone reflection measurement as described in Sec. 4.3.1. The goal of this measurement is to extract the internal Q-factor of the bare horseshoe geometry. Therefore it is appropriate to measure the system in the undercoupled regime, where the internal Q-factor essentially equals the loaded Q-factor. Consequently, the internal Q-factor can be extracted from the reflection spectrum according to Eq. (2.2) and furthermore, the fitting model from Eq. (4.1) can be tested.

The undercoupled regime for the readout mode can be reached by using a retracted antenna. Simulation results show that, for a pin length of $\lesssim 2.3\,\mathrm{mm}$ the loaded

Q-factor is dominated by the internal Q-factor. Therefore the standard commercial antenna[1] without the soldered gold wire is cut to a length of 2.3 mm.

Table 5.1: Simulation and measurement results of the undercoupled horseshoe cavity readout mode without chips. The general agreement is very good.

parameter	simulation	measurement
f_{RO} (GHz)	7.539	7.731
Q_0	$1.06 \cdot 10^6$	$1.86 \cdot 10^6$
Q_{x}	$7.61 \cdot 10^6$	$3.18 \cdot 10^6$
Q_{L}	$9.27 \cdot 10^5$	$1.18 \cdot 10^6$
FWHM (kHz)	7.11	6.58

The results of the reflection measurement fitted to the model from Eq. (4.1) are plotted in Fig. 5.1. A comparison of model parameters and simulation results can be found in Tab. 5.1. Overall, there is a good agreement between simulation and measurements with only minor deviations. The measured resonance frequency of the readout mode of 7.731 GHz is slightly higher than the one expected from the simulation with a value of 7.539 GHz. To some extent this difference can be explained by the shrinking of the material at low temperatures, resulting in an increased frequency [45]. The deviation in internal Q-factors can be attributed to the fact, that CST is not able to simulate a superconductor, thus the simulated surface losses can be higher than in reality. Furthermore, the measured external Q-factor is only about half of the simulated one, which might be caused by fitting errors and a slight position inaccuracy of the antenna. As the difference between the measured values for internal and external Q-factors finally is only about 42 % and not 86 % as in the simulated case, the undercoupled regime, where the internal Q-factor equals the loaded Q-factor is not quite reached in reality. Nevertheless, due to the fitting model, the internal Q-factor can be extracted directly from the measurements without the need of the loaded Q-factor. As a result, the internal Q-factor of the bare horseshoe cavity exceeds one million, which agrees with the state-of-the-art internal Q-factors reached in 3D cavities with typical values of $Q_0 \approx 5 \cdot 10^6$ [46] and $Q_0 \approx 1.5 \cdot 10^6$ for the rectangular cavity at WMI [14]. As a comparison, 2D resonators generally

[1] Rosenberger SMA 32S722-500S5

achieve values of $Q_0 \approx 10^5$ [47] and only by careful fabrication also values above 10^6 [48].

Measurement results of the empty cavity readout mode in the overcoupled regime with the designed antenna from Sec. 4.1.1 are shown in Fig. 5.2. Due to the large difference between internal and external Q-factors, the amplitude response of the cavity is very flat and we use the qualitatively better phase response for fitting. Here, the internal Q-factor is in the same order of magnitude as in the undercoupled case. The low external Q-factor on the order of 10^3 paves the way for a fast readout application.

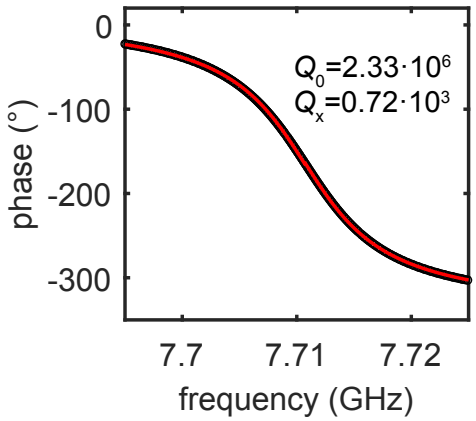

Figure 5.2: Reflection phase of the overcoupled horseshoe cavity readout mode without chips. Eq. (4.1) is fitted (red line) to the measurement data (black dots).

5.2 Horseshoe memory with two qubits

In the following, the horseshoe cavity including the two qubit chips QMv3 2nd and C2 (see Sec. 4.1.2) is measured. In a first step, readout and storage mode are analyzed via a single-tone reflection measurement in the frequency domain and the resonance frequency of the next higher mode is detected. A characterization of the qubit QMv3 2nd in the frequency domain is already done in Sec. 4.3.2 and Sec. 4.3.3. So this part focuses on the qubit characterization in the time domain with the resulting qubit T_1- and T_2-times, the characterization of the BSB transition and finally a discussion of the memory protocol. The second qubit C2 could neither be detected with an AC-Stark measurement nor with a two-tone measurement, so it is assumed to be broken and will be ignored in the following discussion.

5.2.1 Readout, storage and next higher mode

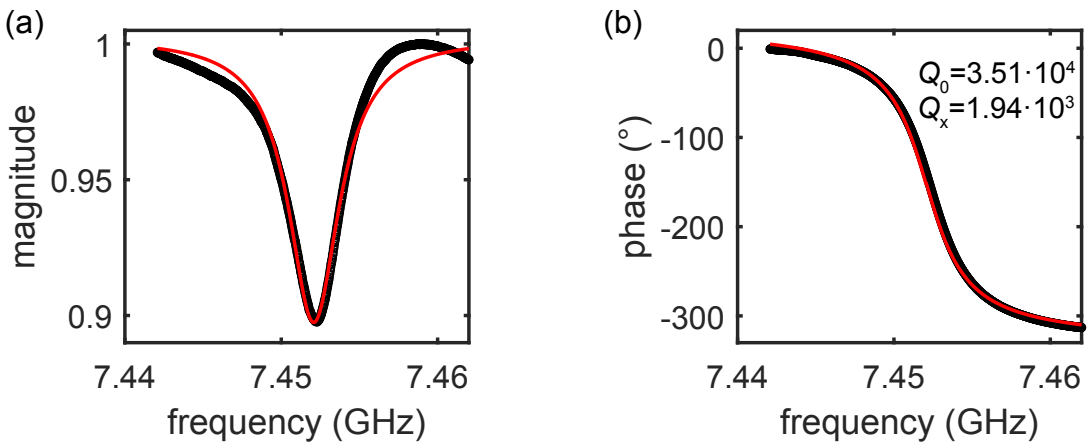

Figure 5.3: Reflection measurement of the horseshoe cavity readout mode with two qubits QMv3 2nd and C2 at a source power of −30 dBm. Eq. (4.1) is fitted (red line) to the measurement data (black dots). (a) Reflection magnitude. (b) Reflection phase.

The bare cavity frequency f_c and the dispersive shift χ_{01} of the readout mode can be extracted from a power sweep of a single-tone measurement as described in Sec. 4.3.1. Together with the qubit parameters from Tab. 4.1, the detuning Δ, the effective dispersive shift χ' and the coupling constant g can be calculated according to Eq. (2.24) and Eq. (2.29).

Figure 5.3 shows the results of a single-tone measurement of the readout mode at a source power of −30 dBm, where the qubit is already decoupled from the mode and the bare readout frequency is detected. To extract the Q-factors of the readout mode, the model from Eq. (4.1) is fitted to the reflected amplitude and phase. Here the phase of the fitting model is unwrapped to fit to the phase response of the VNA. All measured respectively calculated readout mode parameters are summarized in Tab. 5.2.

The storage mode parameters of the cavity are obtained in the same way as the readout mode parameters and are also summarized in Tab. 5.2. A single-tone reflection measurement of the storage mode at −15 dBm, where qubit and mode are decoupled, is plotted in Fig. 5.4. Here the qubit–mode decoupling occurs at higher drive powers than for the readout mode, as the electric field strength E_y at the qubit position and thus the qubit–mode coupling is designed to be stronger for the storage mode (cf. Sec. 3.2.3). This design prediction also agrees with the actually measured

coupling constant g, which is about 50 % higher for the storage mode.

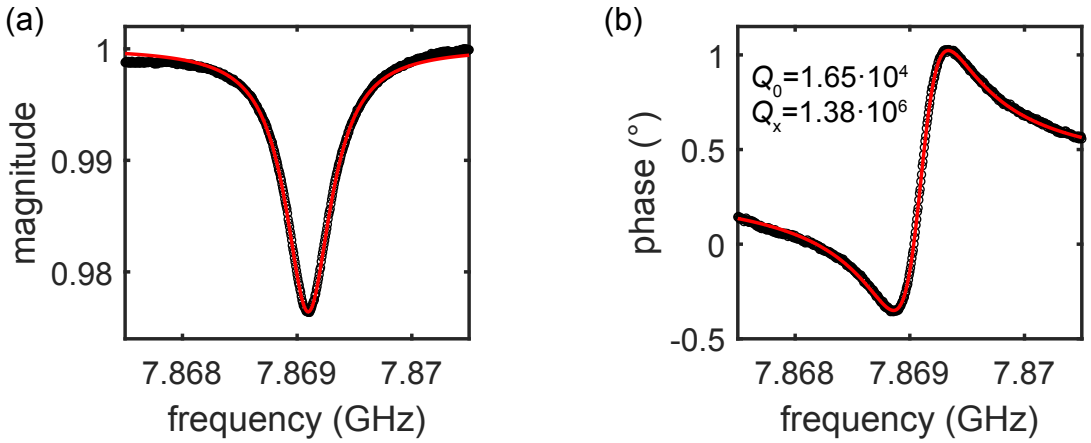

Figure 5.4: Reflection measurement of the horseshoe cavity storage mode with two qubits QMv3 2nd and C2 at a source power of −15 dBm. Eq. (4.1) is fitted (red line) to the measurement data (black dots). (a) Reflection magnitude. (b) Reflection phase.

Comparing the measured cavity frequencies to the ones obtained from simulation (see Sec. 3.2.2) there is a slight deviation of 0.11 GHz for the readout mode and 0.21 GHz for the storage mode, which approximately matches the deviation of 0.19 GHz for the readout mode of the empty cavity (cf. Sec. 5.1). Given these deviations the next higher mode is expected to be around (8.56–8.66) GHz, which fits to the measured mode at 8.616 GHz for a source drive power of −40 dBm. Thus, the measured gap between storage mode and next higher mode is around 750 MHz, which is a factor of 17 larger compared to the rectangular cavity of Refs. [13, 14] (cf. Sec. 3.1).

The measured external Q-factor of the readout mode of $1.94 \cdot 10^3$ matches the order of magnitude from simulation results (see Sec. 3.2.2). Thus the goal of reaching a fast readout is accomplished. Slight deviations of simulation and measurement data can be attributed to fitting errors and a not perfectly accurate antenna positioning. The measured external Q-factor of the storage mode of approximately one million is in the same range as the one reached for the rectangular cavity [14].

The measured internal Q-factors for readout and storage mode are two orders of magnitude lower than for the empty cavity from Sec. 5.1. They are even one order of magnitude lower than the simulated ones for the cavity including lossy silicon chips from Sec. 3.2.3. Thus, the extracted decay time $1/\kappa$ of the storage mode is only given by 0.33 µs. Possible reasons for the low internal Q-factor performance are

examined in Sec. 5.3 and Sec. 5.4. In Sec. 5.3, the not working qubit C2 is replaced by a dummy chip to exclude a perturbation of C2 or its chip. As this approach does not have an impact on the internal Q-factor performance, Sec. 5.4 evaluates the horseshoe cavity with two dummy chips. Here, we can successfully demonstrate that the old qubit chip QMv3 2nd or the qubit QMv3 2nd itself is responsible for the low internal Q-factor and the horseshoe cavity with chips in general reaches internal Q-factors exceeding one million.

Table 5.2: Readout mode and storage mode characterization of the horseshoe cavity with qubits QMv3 2nd and C2.

parameter	readout mode	storage mode
f_{bare} (GHz)	7.4521	7.8691
χ_{01} (MHz)	-1.32	-2.15
χ' (MHz)	-0.586	-0.824
Δ (GHz)	-1.464	-1.881
g (MHz)	43.96	63.59
Q_0	$3.51 \cdot 10^4$	$1.65 \cdot 10^4$
Q_{x}	$1.94 \cdot 10^3$	$1.38 \cdot 10^6$
Q_{L}	$1.84 \cdot 10^3$	$1.63 \cdot 10^4$
$1/\kappa$ (µs)	0.04	0.33

5.2.2 Transmon qubit

The π- and $\pi/2$-pulse length of the transmon qubit are determined via driven Rabi oscillations (see Sec. 4.4.1) to 0.3790 µs respectively 0.1705 µs for a qubit source drive power of -40 dBm. Here, the low source drive power of -40 dBm is chosen to avoid effects due to higher-level excitations and noise. An exemplary Rabi oscillation measurement with a damped sine fit is depicted in Fig. 5.5 (a). Here, the phase denotes the phase of the reflected readout signal, which is 0 for the qubit in the ground state and shifts to more negative values for the qubit in the excited state.
According to Eq. (2.36), the Rabi frequency Ω_{R} is proportional to the drive amplitude Ω_d and thus proportional to the square root of the drive power $\sqrt{P}$. To check up to which power this linear dependence holds, a Rabi oscillation measurement is

performed for different qubit drive powers and the results are plotted in Fig. 5.5 (b). At a drive power of −5 dBm the measurement does not follow the linear fit line anymore, so here higher qubit levels are also excited.

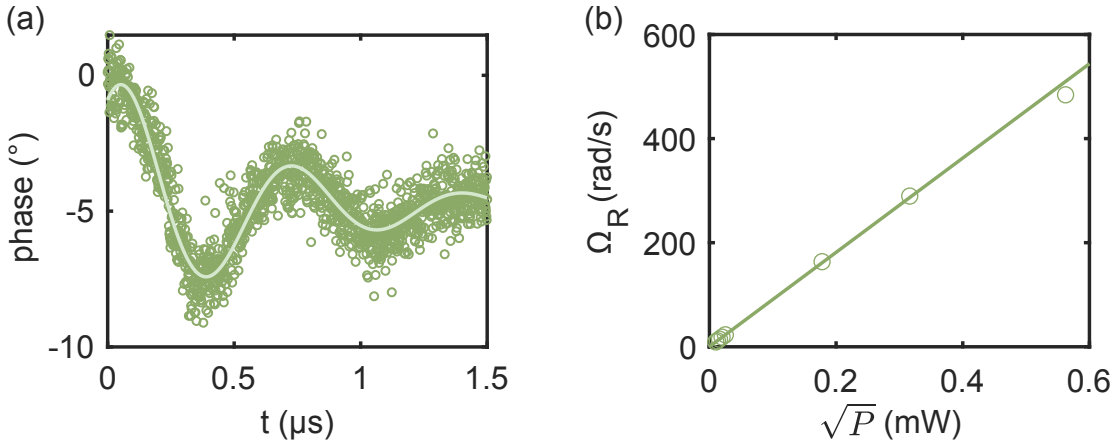

Figure 5.5: (a) Driven Rabi oscillation between ground and excited state of the qubit at a qubit source drive power of −40 dBm. The dots correspond to the measurement data, while the solid line is a damped sine fit. (b) The Rabi frequency Ω_R is plotted over the square root of the qubit source drive power. The last measurement dot at a source power of −5 dBm does not follow the linear fit line anymore.

Qubit relaxation measurements and Ramsey measurements yield average qubit decay times of $T_1^q = (0.48 \pm 0.03)$ µs and $T_2^q = (0.84 \pm 0.08)$ µs. Exemplary measurement results are plotted in Fig. 5.6 (a) and Fig. 5.6 (c) with the corresponding histograms in Fig. 5.6 (b) and Fig. 5.6 (d). From these values, an average dephasing time of $T_\varphi^q = (6.72 \pm 5.90)$ µs can be calculated according to Eq. (2.37) and Gaussian error propagation. Consequently, the qubit coherence is mostly relaxation-limited. The relatively short lifetime of the qubit did not allow for spin echo measurements. A rough estimate of the Purcell decay time according to Eq. (2.38) yields 44 µs for the readout mode and 289 µs for the storage mode. Calculating the Purcell time more accurately with the simulated cavity admittance according to Eq. (2.39) leads to $t_P^{3D} = 48$ µs. Here the CST model includes chips of the material silicon lossy. As the measured qubit T_1-time is considerably below the Purcell time, the system is not Purcell limited.

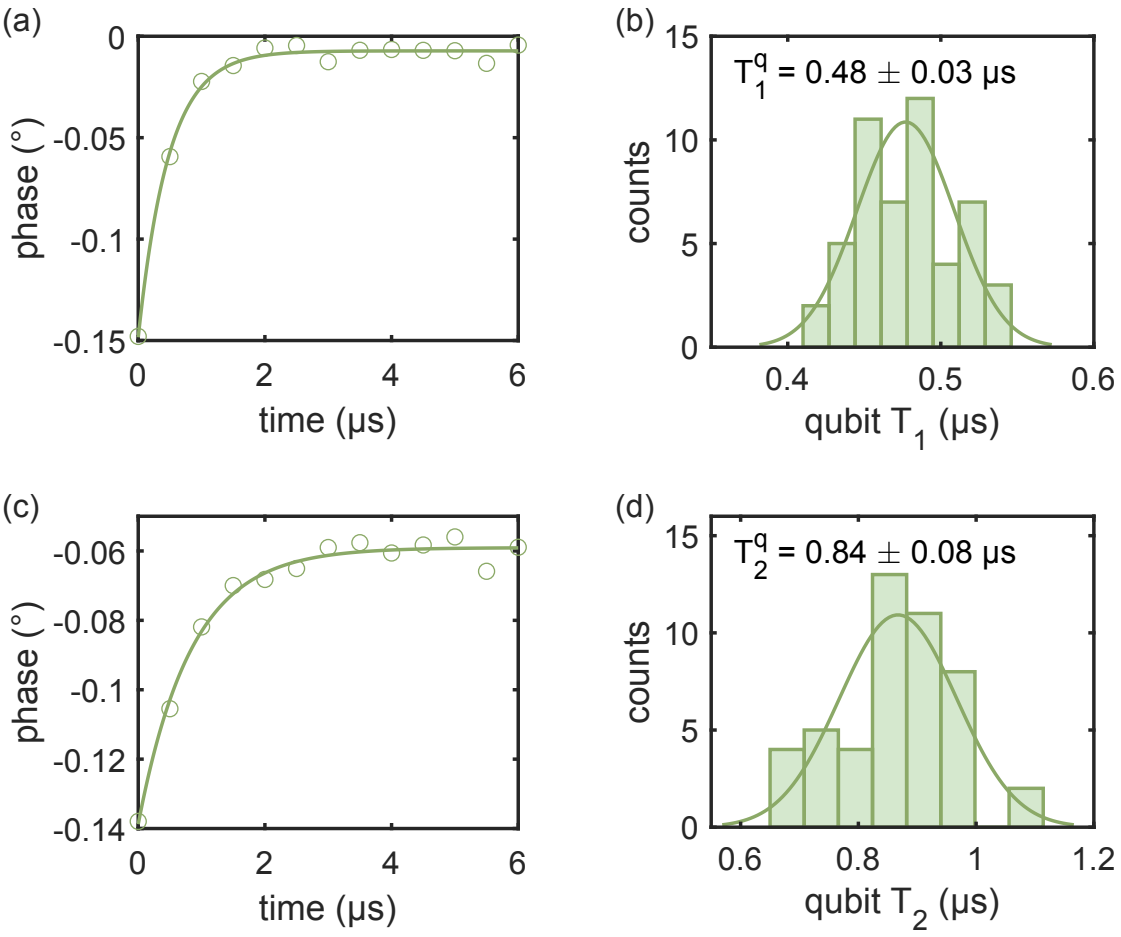

Figure 5.6: Qubit decoherence measurements at a qubit source drive power of −40 dBm. (a) Qubit relaxation measurement according to the protocol of Fig. 4.11 (b). The T_1-time is determined by the exponential fit of the measurement dots. (b) Histogram of the measured qubit T_1-times. (c) Ramsey measurement according to the protocol of Fig. 4.11 (c). The T_2-time is determined by the exponential fit of the measurement dots. (d) Histogram of the measured qubit T_2-times.

5.2.3 BSB transition and memory protocol

In an eigenfrequency measurement (see Sec. 4.4.2), the BSB tranisition frequency is measured for different source drive powers starting from 5 dBm. Then the corresponding Rabi measurements to determine the π-pulse length are performed. For a drive power of 5 dBm, the Rabi oscillation is very noisy, so higher powers are needed for the two-photon process. From a power of 10 dBm on and higher, there seems to be also another excitation apart from the blue sideband, as after the first very

clear oscillation peaks there is only noise. This additional excitation can actually be observed via a two-tone measurement at the corresponding power and frequency, which can be considered as a sideband transition of qubit and an excitation around 8.3 GHz. Possible reasons for the excitation are the accumulation of other two-level systems at the chip's surface as an aging effect or the second qubit chip, that disturbs. Another possibility is, that the next higher mode of the resonator is already at 8.3 GHz, although the mode measured at 8.616 GHz matches the expected frequency. The latter can be excluded from a measurement of the cavity where the second qubit chip is replaced by a dummy chip. Here, there is no mode around 8.3 GHz anymore, so the previous excitation originated from the second qubit chip.

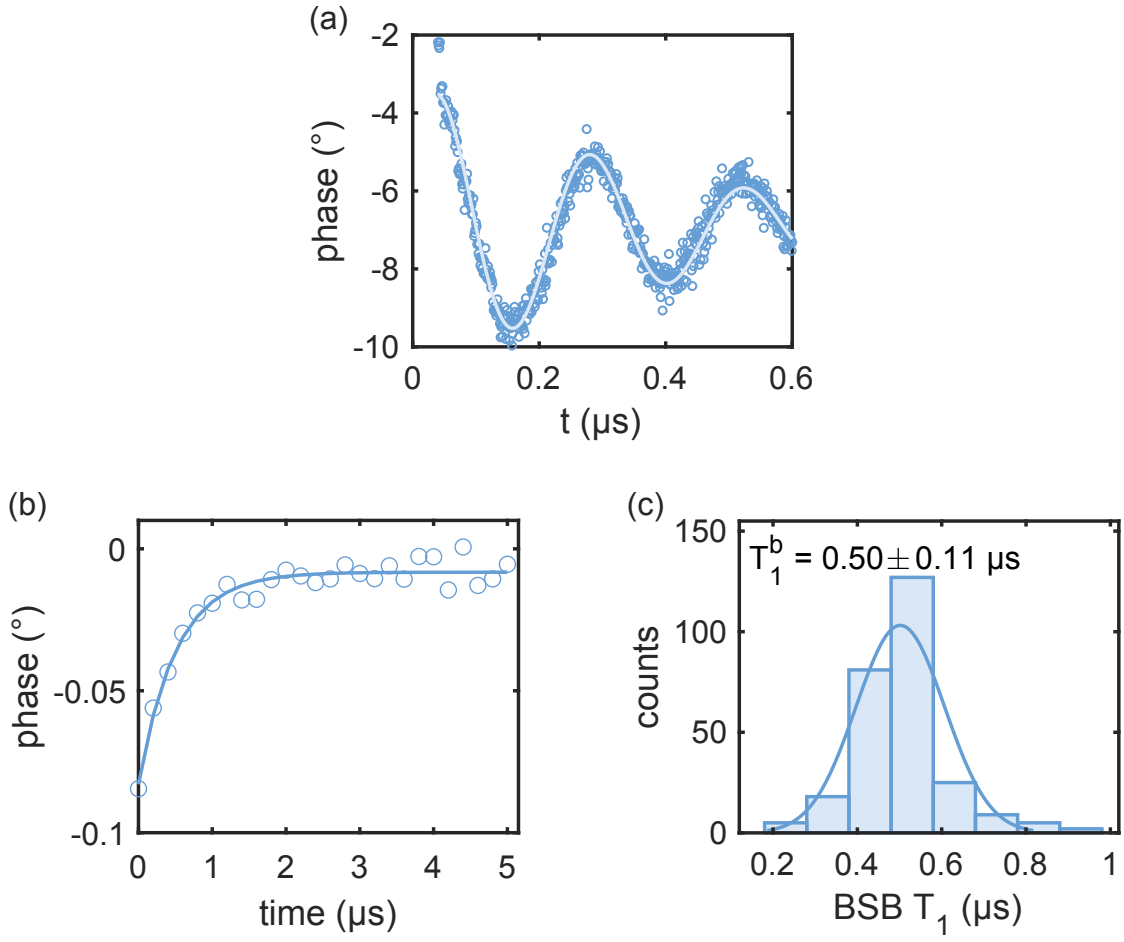

Figure 5.7: Blue sideband measurements at a source drive power of 8 dBm. (a) Driven Rabi oscillation between $|g0\rangle_S$ and $|e1\rangle_S$. (b) BSB relaxation measurement according to the protocol of Fig. 4.12 (c). (c) Histogram of the measured BSB T_1-times.

For the blue sideband transition in the configuration of the cavity with the two qubit chips a drive power of 8 dBm is finally chosen. Here, the Rabi oscillation is not noisy anymore and the additional excitation of the second qubit chip is not present yet. The eigenfrequency measurement yields a BSB transition frequency of $f_\mathrm{b}/2 = 6.8845\,\mathrm{GHz}$ and, from the Rabi measurement of Fig. 5.7 (a), a π-pulse length of 0.157 µs is extracted. The average BSB relaxation time is determined to $T_1^\mathrm{b} = (0.50 \pm 0.11)\,\mu\mathrm{s}$ from the histogram in Fig. 5.7 (c). An exemplary relaxation measurement is shown in Fig. 5.7 (b).

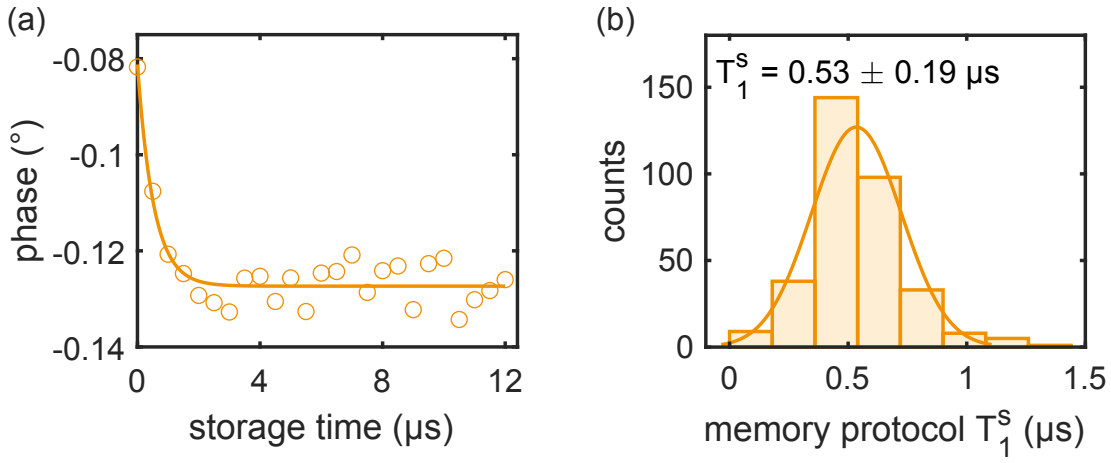

Figure 5.8: (a) Storage time measurement by performing the quantum memory protocol of Fig. 4.12 (d) with exponential fit. (b) Histogram of the measured memory T_1-times.

With the parameters for qubit and BSB π-pulses, the memory protocol (see Sec. 4.4.2) is implemented. Figure 5.8 (a) shows an exemplary measurement of the memory protocol for the ground state being the initial state of the qubit and thus the state to be stored. Histograms for the storage time are depicted in Fig. 5.8 (b), resulting in $T_1^\mathrm{s} = (0.53 \pm 0.19)\,\mu\mathrm{s}$. Thus, we find that the storage time is similar to the qubit T_1-time.

5.3 Horseshoe memory with one qubit and one dummy chip

As the qubit C2 from Sec. 5.2 is most probably broken, it is replaced by a dummy chip in another cooldown. Thus the horseshoe cavity with the qubit QMv3 2$^\mathrm{nd}$ can be examined without a possible perturbation of qubit C2.

5.3.1 Readout mode

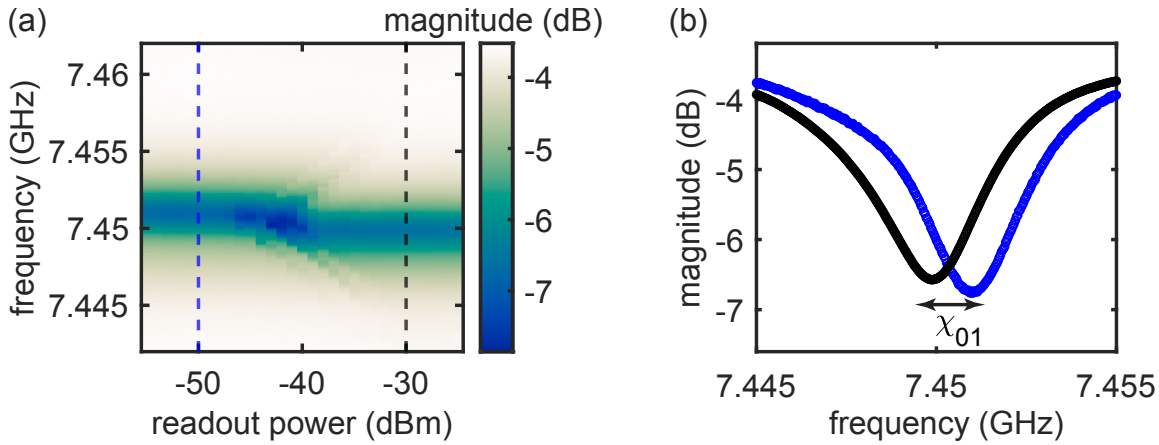

Figure 5.9: Single-tone measurement of the readout mode (horseshoe memory with one qubit and one dummy chip). (a) The reflection magnitude is plotted as a function of drive frequency and power. The blue and black vertical cuts at $-50\,\mathrm{dBm}$ respectively $-30\,\mathrm{dBm}$ are shown in (b).

The dispersive shift of qubit and readout mode is extracted from a power sweep of the readout signal (cf. Fig. 5.9). Here, the small deviation in the depth of the resonance dips in Fig. 5.9 (b) can be attributed to the frequency-dependent gain of the amplification chain (cf. Sec. 4.2.3). The measured dispersive shift of $\chi_{01}^{\mathrm{RO}} = -1.10\,\mathrm{MHz}$ is only 5/6 from the value of the previous cooldown for the cavity with qubit QMv3 2nd and C2 (see Sec. 5.2). Assuming that the coupling constant g has not changed, a difference in the qubit–mode detuning Δ has to be responsible for the reduction of the shift [cf. Eq. (2.29)]. The bare mode frequency at $-30\,\mathrm{dBm}$ is extracted from Fig. 5.10 to 7.4498 GHz, which is 2.3 MHz lower than for the cavity with QMv3 2nd and C2. Thus the qubit frequency f_{q} is estimated to be around 5.6930 GHz, which is a reduction of approximately 0.30 GHz, compared to the previous cooldown. This reduction can be explained by the aging effect of the transmon qubit once it is exposed to air [14, 49], which inevitably happened between the two cooldowns. In order to measure the actual qubit transition frequency, an AC-Stark and a two-tone measurement are performed. The measurement results do not show any phase shift in the readout signal, although the qubit drive frequency is swept from (5–6) GHz. So, within the scope of this thesis, it is not possible to find the qubit transition frequency anymore, which may be caused by a further deterioration of the qubit coherence.

The Q-factors and the decay time of the readout mode are extracted from the data

shown in Fig. 5.10 and summarized in Tab. 5.3. Except for negligible deviations due to fitting errors, they are in accordance with the values of the cavity with qubit QMv3 2nd and C2 from Tab. 5.2. As a result, the source of the unforeseen low memory lifetime is expected to be caused by the qubit QMv3 2nd or its chip.

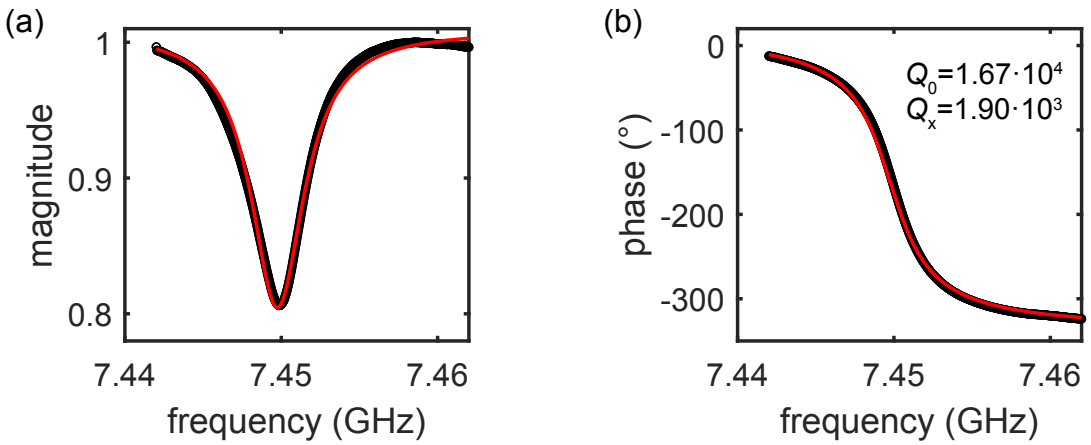

Figure 5.10: Reflection measurement of the horseshoe cavity readout mode with qubit QMv3 2nd and a dummy chip at a source power of −30 dBm. Eq. (4.1) is fitted (red line) to the measurement data (black dots). (a) Reflection magnitude. (b) Reflection phase.

5.3.2 Storage mode

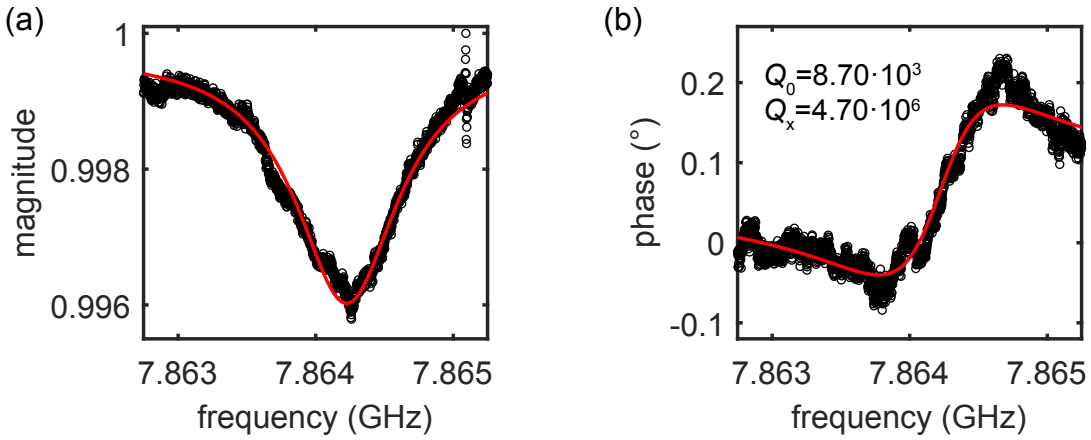

Figure 5.11: Reflection measurement of the horseshoe cavity storage mode with qubit QMv3 2nd and a dummy chip at a source power of −15 dBm. Eq. (4.1) is fitted (red line) to the measurement data (black dots). (a) Reflection magnitude. (b) Reflection phase.

The parameters for the storage mode extracted from Fig. 5.11 are summarized in Tab. 5.2. The bare resonance frequency at 7.8642 GHz is 4.9 MHz lower than the one measured for the cavity with two qubits. The internal Q-factor decreased by 40 %, while the external Q-factor nearly increased by a factor of 3. In part these deviations can certainly be attributed to fit imprecision, but nevertheless the order of magnitude has not changed. One can conclude, that the total Q-factor performance of the storage mode is limited by the internal Q-factor, which is approximately two orders of magnitude lower than the external one.

Table 5.3: Readout mode and storage mode characterization of the horseshoe cavity with qubit QMv3 2nd and a dummy chip.

parameter	readout mode	storage mode
f_{bare} (GHz)	7.4498	7.8642
Q_0	$1.67 \cdot 10^4$	$8.70 \cdot 10^3$
Q_{x}	$1.90 \cdot 10^3$	$4.70 \cdot 10^6$
Q_{L}	$1.70 \cdot 10^3$	$8.69 \cdot 10^3$
$1/\kappa$ (µs)	0.04	0.18

5.4 Horseshoe memory with two dummy chips

To investigate the reason for the low internal Q-factor performance of the horseshoe with qubit chips from Sec. 5.2 and Sec. 5.3, the horseshoe cavity is measured with two dummy chips in another cooldown. Thus it can be inferred more directly, whether the chip insertion in general or the special qubit chip with qubit QMv3 2nd is responsible for the internal Q-factor reduction by two orders of magnitude compared to the empty cavity.
Due to the crosstalk between the cables or the coupling structures, the reflected raw data contains background structure. One possibility to account for this background is to add a complex translation to the reflection coefficient from Eq. (4.1):

$$\Gamma' = \Gamma + x + iy, \tag{5.1}$$

resulting in two additional fitting parameters [50, 51]. This is done for the reflection magnitude in Fig. 5.12 after a linear fit of the first data points has been subtracted

from the raw data. Another possibility to account for the background is to subtract a linear trend and thus symmetrize the reflection dip. Then, Eq. (4.1) can be fitted to the magnitude or phase of the reflection coefficient, as depicted in Fig. 5.13.

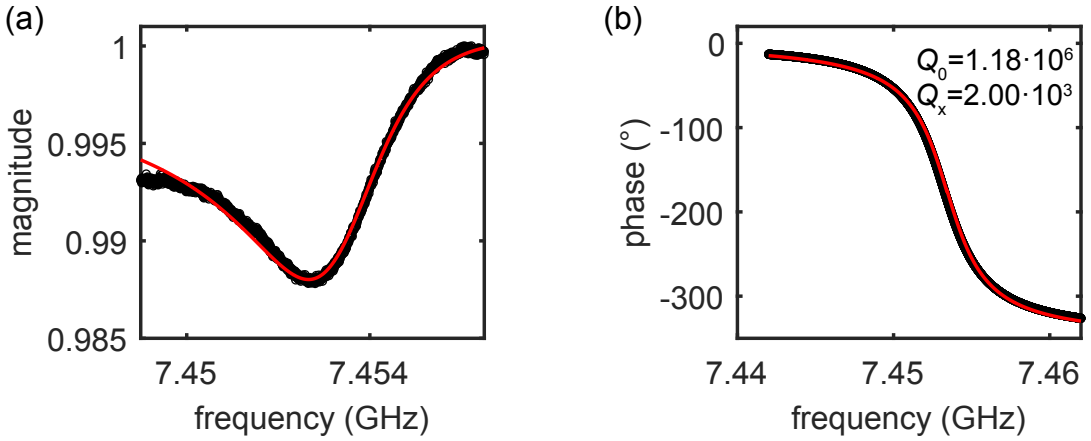

Figure 5.12: Reflection measurement of the horseshoe cavity readout mode with two dummy chips at a source power of −30 dBm. Eq. (5.1) is fitted (red line) to the measurement data (black dots). A linear fit of the first data points has been subtracted from the raw data. (a) Reflection magnitude. (b) Reflection phase.

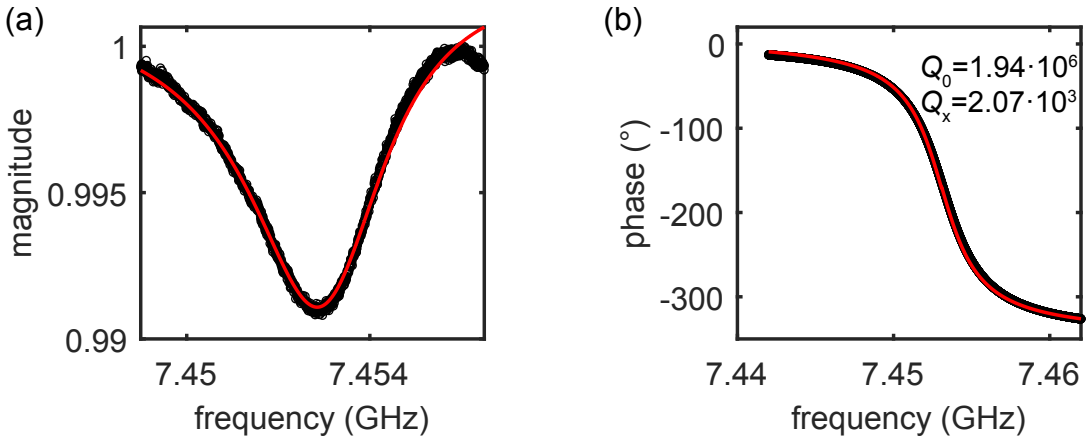

Figure 5.13: Reflection measurement of the horseshoe cavity readout mode with two dummy chips at a source power of −30 dBm. Eq. (4.1) is fitted (red line) to the measurement data (black dots). A linear trend has been subtracted from the raw data. (a) Reflection magnitude. (b) Reflection phase.

The resulting resonance frequency, Q-factors and decay time extracted from the two fitting models are summarized in Tab. 5.4. The results agree very well with each other. The main result of this measurement is the high internal Q-factor exceeding one million, which is the same order of magnitude as for the empty horseshoe cavity. So one can conclude that the cavity design discussed in this thesis actually works fine and the qubit chip with qubit QMv3 2nd or the qubit QMv3 2nd itself has been responsible for the low internal Q-factor performance of the cavity. With the external Q-factor of the storage mode from Tab. 5.3 and the measured internal Q-factor for the readout mode in this section, we expect a FWHM of approximately 6 kHz for the storage mode. This value corresponds to a storage time of 27 µs. In the scope of this thesis, it has not been possible to actually find the storage mode in this configuration with direct VNA measurements, although we explore a frequency range of ±30 MHz around the expected resonance frequency from Tab. 5.3 with a maximal step width of 0.5 kHz. As the frequency of the readout mode is only shifted by 3 MHz, the storage mode frequency is expected to be in the measured range. Since a strongly undercoupled mode is expected to be difficult to detect with a direct VNA measurement, our result supports the assumption that the Q-factor of the storage mode is in principle high and has only been reduced due to the presence of the QMv3 2nd qubit chip. In other words, the above results suggest that a long-lived quantum memory is not at all forbidden by design restrictions, but can be straightforwardly implemented with a better qubit chip.

Table 5.4: Readout mode characterization of the horseshoe cavity with two dummy chips.

parameter	readout mode asymmetric	readout mode symmetric
f_{bare} (GHz)	7.4534	7.4531
Q_0	$1.18 \cdot 10^6$	$1.94 \cdot 10^6$
Q_{x}	$2.00 \cdot 10^3$	$2.07 \cdot 10^3$
Q_{L}	$1.99 \cdot 10^3$	$2.07 \cdot 10^3$
$1/\kappa$ (µs)	0.04	0.04

Future measurements to find the storage mode could be performed by inserting a branched antenna pin, that expands to the left and right of the recess to lower the external Q-factor. From such a measurement the internal Q-factor of the storage mode can be extracted and the range of the resonance frequency can be restricted. Then, the next step consists in actually measuring the storage mode with the normal pin, confirming the high storage time and eventually test the horseshoe quantum memory with another qubit.

Chapter 6

Conclusions and Outlook

In this thesis a novel geometry for a compact 3D quantum memory has been designed, optimized, and experimentally investigated for the applications in the emerging field of quantum technologies.
The goal to optimize the horseshoe cavity design with respect to fast readout and long storage times has been reached with finite-element simulations. Therefore the cavity parameters have been designed in such a way that the readout mode couples strongly to the antenna port reaching a low external Q-factor of magnitude 10^3. Simultaneously, the storage mode, which mainly lives in the arms of the horseshoe geometry, is expected to reach an external Q-factor on the order of 10^{12} for a perfectly positioned antenna. Due to the beneficial mode structure of readout and storage mode, the horseshoe design allows for an antenna position inaccuracy in y-direction of $\pm 0.53\,\mathrm{mm}$ to still reach an external Q-factor of 10^6 for the storage mode. This tolerance is an improvement by a factor of four compared to a rectangular geometry [14]. Furthermore, it has been shown that even a tilt of 10° of the antenna pin barely has any influence on the external Q-factor performance of the storage mode.
In experiment, it has been shown that the internal Q-factor of the empty cavity exceeds one million without any surface treatment. This order of magnitude also agrees with simulation results. In order to even increase the internal Q-factor in future measurements, the aluminum cavity could be electropolished [45] or treated with acid [52] to decrease surface losses. Such a treatment increases the internal Q-factor by at least one order of magnitude. In addition, we have shown that the internal Q-factor is not reduced by inserting dummy chips. Equally important, our measurements indicate that the external Q-factor of the storage mode is currently neither limited by the antenna placement accuracy nor by field distortions due to the presence of the dummy chips.

The measured frequency gap between storage mode and next higher mode around 750 MHz matches the simulation results and is a factor of 17 larger compared to a rectangular cavity design. This is beneficial since now an undesired excitation of the next higher mode is unlikely.

Paving the way towards a fast readout, a low external Q-factor of approximately $2 \cdot 10^3$ for the readout mode has been measured. Unexpectedly, the insertion of the qubit chips has caused the internal Q-factor of readout and storage mode to decrease by two orders of magnitude, resulting in a Q_0 on the order of 10^4. Thus, the performance of the current memory device (which requires the presence of a qubit) has been limited by the internal Q-factor. Decay times of 0.04 µs for the readout mode and 0.33 µs for the storage mode have been measured in frequency domain measurements.

Besides the characterization of the horseshoe geometry, it has been possible to measure the parameters of qubit QMv3 2$^{\text{nd}}$, the blue sideband transition and finally to implement the quantum memory protocol in the horseshoe cavity. Qubit decoherence times of $T_1^{\text{q}} = (0.48 \pm 0.03)$ µs and $T_2^{\text{q}} = (0.84 \pm 0.08)$ µs have been extracted. In comparison to previous measurements in 2018 [14], the qubit decoherence times decreased by 2/3, which can be attributed to aging. Statistics on the quantum memory protocol yield storage times of $T_1^{\text{s}} = (0.53 \pm 0.19)$ µs, which match the frequency domain measurements. Due to the low internal Q-factor resulting from the insertion of the qubit QMv3 2$^{\text{nd}}$, these storage times unfortunately do not exceed the qubit decay time in the current device. However, when the designed horseshoe cavity is measured with a new qubit, more promising storage times are expected.

In the future, a possible next step consists in increasing the external Q-factor of the storage mode for the horseshoe configuration with two dummy chips in a controlled way by suitably modifying the antenna. In this way, the lifetime of the storage mode could be measured in a more direct way as compared to the current work. Ultimately, the horseshoe architecture has to be tested with a freshly fabricated transmon qubit. When fabricating the new qubit, one could think about a surface treatment of the silicon substrate to improve the internal Q-factor [53, 54]. From a design point of view, further simulations can explore a possible effect of the qubit design on the storage mode properties.

Appendix A

Transformation of driven qubit-resonator Hamiltonian

In Sec. 2.3.3, the Hamiltonian of a driven qubit-resonator system

$$\hat{H} = \hbar\omega_{\mathrm{c}}\hat{a}^{\dagger}\hat{a} + \frac{\hbar\omega_{\mathrm{q}}}{2}\hat{\sigma}_{\mathrm{z}} + \hbar g(\hat{a}\hat{\sigma}_{+} + \hat{a}^{\dagger}\hat{\sigma}_{-}) + \hbar\Omega_{\mathrm{d}}(\hat{a}^{\dagger}e^{-i\omega_{\mathrm{d}}t} + \hat{a}e^{+i\omega_{\mathrm{d}}t}) \tag{A.1}$$

(here the zero-point energy of the resonator is neglected) is transformed to a displaced frame as

$$\hat{H} \rightarrow \hat{D}\hat{H}\hat{D}^{\dagger} + i\hbar\dot{\hat{D}}\hat{D}^{\dagger}. \tag{A.2}$$

To evaluate the first term in Eq. (A.2) the Hadamard lemma

$$e^{\hat{x}}\hat{y}e^{-\hat{x}} = \hat{y} + [\hat{x}, \hat{y}] + ..., \tag{A.3}$$

with $\hat{x} = \alpha\hat{a}^{\dagger} - \alpha^{*}\hat{a}$ is applied to the Hamiltonian. The following commutator relations are used during the calculation:

$$[\hat{a}, \hat{a}^{\dagger}] = 1, \tag{A.4}$$

$$[\hat{x}, \hat{a}^{\dagger}\hat{a}] = -\alpha\hat{a}^{\dagger} - \alpha^{*}\hat{a}, \tag{A.5}$$

$$[\hat{x}, \hat{a}^{\dagger}] = -\alpha^{*}, \tag{A.6}$$

$$[\hat{x}, \hat{a}] = -\alpha. \tag{A.7}$$

Then, the first term in Eq. (A.2) applied to each part of the Hamiltonian separately gives:

$$\begin{aligned}\hat{D}\hat{H}\hat{D}^\dagger =& \hbar\omega_\mathrm{c}\hat{a}^\dagger\hat{a} + \hbar\omega_\mathrm{c}(-\alpha\hat{a}^\dagger - \alpha^*\hat{a}) + \\ & \frac{\hbar\omega_\mathrm{q}}{2}\hat{\sigma}_z + \\ & \hbar g(\hat{a}\hat{\sigma}_+ + \hat{a}^\dagger\hat{\sigma}_-) + \hbar g(-\alpha\hat{\sigma}_+ - \alpha^*\hat{\sigma}_-) + \\ & \hbar\Omega_\mathrm{d}((\hat{a}^\dagger - \alpha^*)e^{-i\omega_\mathrm{d}t} + (\hat{a} - \alpha)e^{i\omega_\mathrm{d}t}. \end{aligned} \tag{A.8}$$

The second term in Eq. (A.2) gives:

$$i\hbar\dot{\hat{D}}\hat{D}^\dagger = i\hbar\dot{\hat{x}}\underbrace{e^{\hat{x}}e^{-\hat{x}}}_{=1} = i\hbar(\dot{\alpha}\hat{a}^\dagger - \dot{\alpha^*}\hat{a}), \tag{A.9}$$

where the Baker-Campbell-Hausdorff formula is used to show that $\hat{x}e^{-\hat{x}} = 1$. To reach the desired form of the transformed Hamiltonian from Eq. (2.34) the remaining terms from Eq. (A.8) and Eq. (A.9) have to cancel each other:

$$\hbar\omega_\mathrm{c}(-\alpha\hat{a}^\dagger - \alpha^*\hat{a}) + i\hbar(\dot{\alpha}\hat{a}^\dagger - \dot{\alpha^*}\hat{a}) + \hbar\Omega_\mathrm{d}((\hat{a}^\dagger - \alpha^*)e^{-i\omega_\mathrm{d}t} + (\hat{a} - \alpha)e^{i\omega_\mathrm{d}t} = 0. \tag{A.10}$$

Selecting the coefficients associated with $\hat{a}^\dagger$ and $\hat{a}$ leads to the ordinary differential equation for α:

$$\dot{\alpha} = -i\omega_\mathrm{c}\alpha + i\Omega_\mathrm{d}e^{-i\omega_\mathrm{d}t}. \tag{A.11}$$

Appendix B

CAD drawing

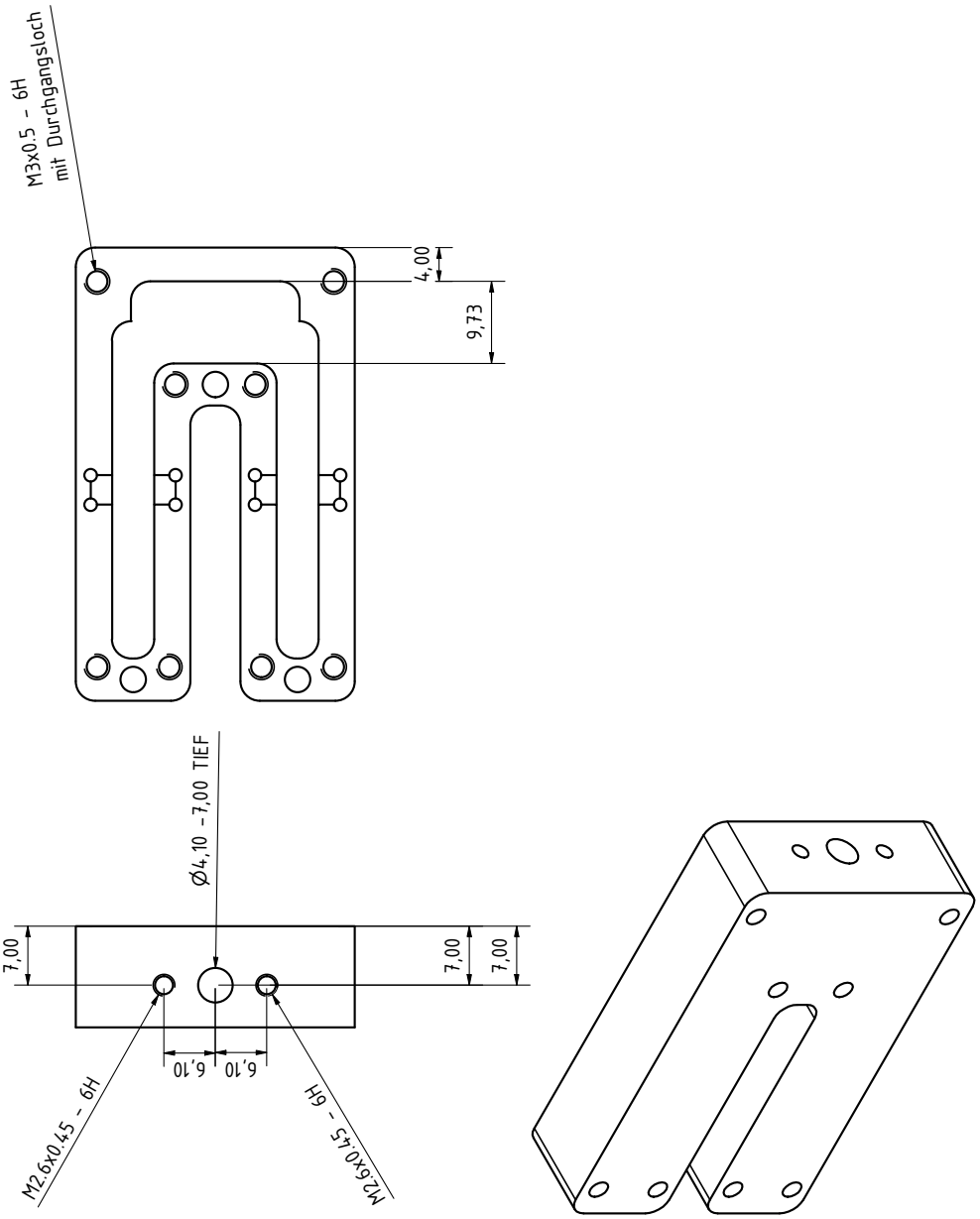

Figure B.1: CAD drawing of the upper cavity half.

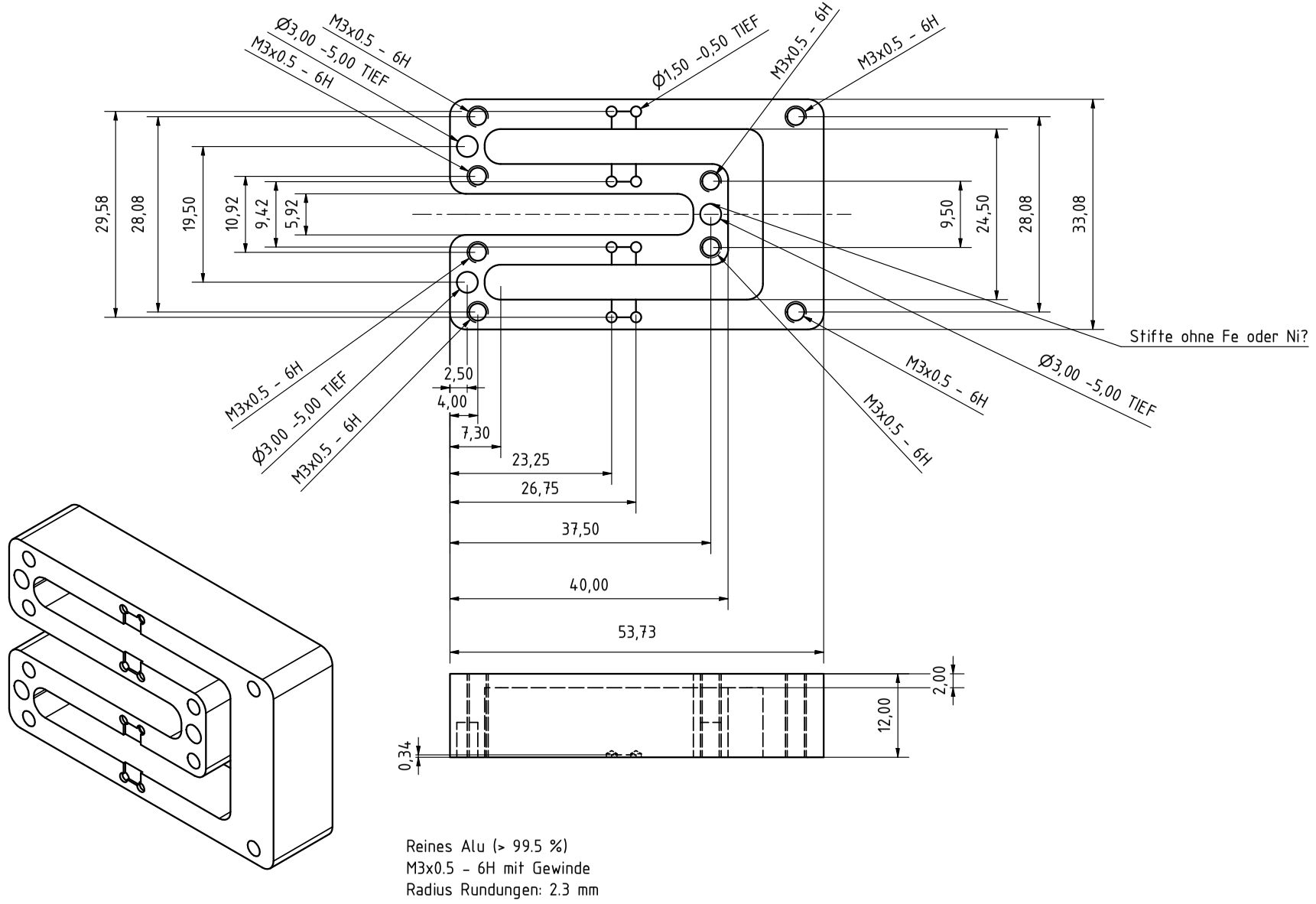

Figure B.2: CAD drawing of the lower cavity half.

Bibliography

[1] R. Rojas, "The Z1: Architecture and Algorithms of Konrad Zuse's First Computer", CoRR:1406.1886 (2014).

[2] P. W. Shor, "Polynomial-Time Algorithms for Prime Factorization and Discrete Logarithms on a Quantum Computer", SIAM Journal on Computing **26**, 1484–1509 (1997).

[3] B. e. a. Arute, Arya, "Quantum supremacy using a programmable superconducting processor.", Nature **574**, 505 (2019).

[4] A. Fruchtman and I. Choi, "Technical Roadmap for Fault-Tolerant Quantum Computing", (2016), URL `https://nqit.ox.ac.uk/content/technical-roadmap-fault-tolerant-quantum-computing.html`.

[5] M. Schlosshauer, "Decoherence, the measurement problem, and interpretations of quantum mechanics", Rev. Mod. Phys. **76** (2005).

[6] M. H. Devoret and R. J. Schoelkopf, "Superconducting Circuits for Quantum Information: An Outlook", Science **339**, 1169 (2013).

[7] R. Di Candia, K. Fedorov, L. Zhong, S. Felicetti, E. Menzel, M. Sanz, F. Deppe, A. Marx, R. Gross, and E. Solano, "Quantum teleportation of propagating quantum microwaves", EPJ Quantum Technology **2** (2015).

[8] S. Pogorzalek, K. G. Fedorov, M. Xu, A. Parra-Rodriguez, M. Sanz, M. Fischer, E. Xie, K. Inomata, Y. Nakamura, E. Solano, A. Marx, F. Deppe, and R. Gross, "Secure quantum remote state preparation of squeezed microwave states", Nat. Commun. **10**, 2604 (2019).

[9] V. Scarani and C. Kurtsiefer, "The black paper of quantum cryptography: real implementation problems", (2009), `0906.4547`.

[10] A. Wallraff, D. I. Schuster, A. Blais, L. Frunzio, R.-S. Huang, J. Majer, S. Kumar, S. M. Girvin, and R. J. Schoelkopf, "Strong coupling of a single photon to

a superconducting qubit using circuit quantum electrodynamics", Nature **431**, 162 (2004).

[11] A. Blais, R.-S. Huang, A. Wallraff, S. M. Girvin, and R. J. Schoelkopf, "Cavity quantum electrodynamics for superconducting electrical circuits: An architecture for quantum computation", Phys. Rev. A **69** (2004).

[12] W. Wang, L. Hu, Y. Xu, K. Liu, Y. Ma, S.-B. Zheng, R. Vijay, Y. P. Song, L.-M. Duan, and L. Sun, "Converting Quasiclassical States into Arbitrary Fock State Superpositions in a Superconducting Circuit", Phys. Rev. Lett. **118**, 223604 (2017).

[13] E. Xie, F. Deppe, M. Renger, D. Repp, P. Eder, M. Fischer, J. Goetz, S. Pogorzalek, K. G. Fedorov, A. Marx, and et al., "Compact 3D quantum memory", Applied Physics Letters **112**, 202601 (2018).

[14] E. Xie, "A scalable 3D quantum memory", Ph.D. thesis, TU München (2018), URL https://www.wmi.badw.de/publications/theses/Xie,Edwar_Doktorarbeit_2019.pdf.

[15] M. Reagor, W. Pfaff, C. Axline, R. W. Heeres, N. Ofek, K. Sliwa, E. Holland, C. Wang, J. Blumoff, K. Chou, M. J. Hatridge, L. Frunzio, M. H. Devoret, L. Jiang, and R. J. Schoelkopf, "Quantum memory with millisecond coherence in circuit QED", Phys. Rev. B **94**, 014506 (2016).

[16] D. M. Pozar, *Microwave Engineering* (John Wiley & Sons, Inc., 2012).

[17] CST STUDIO SUITE www.cst.com.

[18] S. M. Girvin, *Circuit QED: superconducting qubits coupled to microwave photons* (Oxford University Press, 2014).

[19] D. P. DiVincenzo, "The Physical Implementation of Quantum Computation", Fortschr. Phys. **48**, 771–783 (2000).

[20] R. Han, N. Lörch, J. Suzuki, and B.-G. Englert, "Long-lived qubit from three spin-12atoms", Phys. Rev. A **84** (2011).

[21] M. Gündoğan, P. M. Ledingham, A. Almasi, M. Cristiani, and H. de Riedmatten, "Quantum Storage of a Photonic Polarization Qubit in a Solid", Phys. Rev. Lett. **108** (2012).

[22] M. A. Nielsen and I. L. Chuang, *Quantum Computation and Quantum Information: 10th Anniversary Edition* (Cambridge University Press, 2010).

[23] R. Gross and A. Marx, *Festkörperphysik* (De Gruyter, 2014).

[24] J. A. Schreier, A. A. Houck, J. Koch, D. I. Schuster, B. R. Johnson, J. M. Chow, J. M. Gambetta, J. Majer, L. Frunzio, M. H. Devoret, and et al., "Suppressing charge noise decoherence in superconducting charge qubits", Phys. Rev. B **77** (2008).

[25] A. A. Houck, J. Koch, M. H. Devoret, S. M. Girvin, and R. J. Schoelkopf, "Life after charge noise: recent results with transmon qubits", Quantum Information Processing **8**, 105 (2009).

[26] J. Koch, T. M. Yu, J. Gambetta, A. A. Houck, D. I. Schuster, J. Majer, A. Blais, M. H. Devoret, S. M. Girvin, and R. J. Schoelkopf, "Charge-insensitive qubit design derived from the Cooper pair box", Phys. Rev. A **76** (2007).

[27] A. Wallraff, D. I. Schuster, A. Blais, L. Frunzio, J. Majer, M. H. Devoret, S. M. Girvin, and R. J. Schoelkopf, "Approaching Unit Visibility for Control of a Superconducting Qubit with Dispersive Readout", Phys. Rev. Lett. **95**, 060501 (2005).

[28] D. I. Schuster, A. Wallraff, A. Blais, L. Frunzio, R.-S. Huang, J. Majer, S. M. Girvin, and R. J. Schoelkopf, "ac Stark Shift and Dephasing of a Superconducting Qubit Strongly Coupled to a Cavity Field", Phys. Rev. Lett. **94** (2005).

[29] A. Blais, J. Gambetta, A. Wallraff, D. I. Schuster, S. M. Girvin, M. H. Devoret, and R. J. Schoelkopf, "Quantum-information processing with circuit quantum electrodynamics", Phys. Rev. A **75**, 032329 (2007).

[30] C. J. Axline, "Building Blocks for Modular Circuit QED Quantum Computing", Ph.D. thesis, Yale University (2018), URL https://rsl.yale.edu/sites/default/files/files/Chris%20Axline%20-%20Thesis%20-%20smaller.pdf.

[31] M. O. Scully and M. S. Zubairy, *Quantum Optics* (Cambridge University Press, 1997).

[32] A. Wallraff, D. I. Schuster, A. Blais, J. M. Gambetta, J. Schreier, L. Frunzio, M. H. Devoret, S. M. Girvin, and R. J. Schoelkopf, "Sideband Transitions and

Two-Tone Spectroscopy of a Superconducting Qubit Strongly Coupled to an On-Chip Cavity", Phys. Rev. Lett. **99** (2007).

[33] F. Deppe, M. Mariantoni, E. P. Menzel, A. Marx, S. Saito, K. Kakuyanagi, T. Meno, K. Semba, H. Takayanagi, E. Solano, and R. Gross, "Two-photon probe of the Jaynes-Cummings model and controlled symmetry breaking in circuit QED", Nature Phys. **4**, 686 (2008).

[34] J. Goetz, F. Deppe, K. G. Fedorov, P. Eder, M. Fischer, S. Pogorzalek, E. Xie, A. Marx, and R. Gross, "Parity-Engineered Light-Matter Interaction", Phys. Rev. Lett. **121**, 060503 (2018).

[35] A. Abragam, *The Principles of Nuclear Magnetism* (Oxford University Press, 1961).

[36] H. et al., "Controlling the Spontaneous Emission of a Superconducting Transmon Qubit", Phys. Rev. Lett. **101** (2008).

[37] K. L. Geerlings, "Improving Coherence of Superconducting Qubits and ResonatorsImproving Coherence of Superconducting Qubits and Resonators", Ph.D. thesis, Yale University (2013), URL https://qulab.eng.yale.edu/documents/theses/Kurtis_ImprovingCoherenceSuperconductingQubits.pdf.

[38] J. Goetz, "The Interplay of Superconducting Quantum Circuits and Propagating Microwave States", Ph.D. thesis, Technische Universität München (2017), URL http://www.wmi.badw.de/publications/theses/Goetz,Jan_Doktorarbeit_2017_TUM.pdf.

[39] D. Schuster, "Circuit Quantum Electrodynamics", Ph.D. thesis, Yale University (2007), URL https://rsl.yale.edu/sites/default/files/files/RSL_Theses/SchusterThesis.pdf.

[40] S. Trattnig, "Quantum Memory with Optimal Control", Master's thesis, TU München (2020).

[41] M. Pierre, S. R. Sathyamoorthy, I.-M. Svensson, G. Johansson, and P. Delsing, "Resonant and off-resonant microwave signal manipulation in coupled superconducting resonators", Phys. Rev. B **99** (2019).

[42] M. D. Reed, L. DiCarlo, B. R. Johnson, L. Sun, D. I. Schuster, L. Frunzio, and R. J. Schoelkopf, "High-Fidelity Readout in Circuit Quantum Electrodynamics Using the Jaynes-Cummings Nonlinearity", Phys. Rev. Lett. **105**, 173601 (2010).

[43] S. M. Anton, C. Müller, J. S. Birenbaum, S. R. O'Kelley, A. D. Fefferman, D. S. Golubev, G. C. Hilton, H.-M. Cho, K. D. Irwin, F. C. Wellstood, G. Schön, A. Shnirman, and J. Clarke, "Pure dephasing in flux qubits due to flux noise with spectral density scaling as $1/f^{\alpha}$", Phys. Rev. B **85**, 224505 (2012).

[44] P. J. Leek, M. Baur, J. M. Fink, R. Bianchetti, L. Steffen, S. Filipp, and A. Wallraff, "Cavity Quantum Electrodynamics with Separate Photon Storage and Qubit Readout Modes", Phys. Rev. Lett. **104**, 100504 (2010).

[45] J. R. A. Müller, "3D Cavities for Circuit Quantum Electrodynamics", Bachelor's thesis, TU München (2014), URL https://www.wmi.badw.de/publications/theses/Mueller,Jonathan%20Bachelor%20Thesis%202014.pdf.

[46] H. Paik, D. I. Schuster, L. S. Bishop, G. Kirchmair, G. Catelani, A. P. Sears, B. R. Johnson, M. J. Reagor, L. Frunzio, L. I. Glazman, S. M. Girvin, M. H. Devoret, and R. J. Schoelkopf, "Observation of High Coherence in Josephson Junction Qubits Measured in a Three-Dimensional Circuit QED Architecture", Phys. Rev. Lett. **107**, 240501 (2011).

[47] A. Blais, A. L. Grimsmo, S. M. Girvin, and A. Wallraff, "Circuit Quantum Electrodynamics", (2020), 2005.12667.

[48] A. Bruno, G. de Lange, S. Asaad, K. L. van der Enden, N. K. Langford, and L. DiCarlo, "Reducing intrinsic loss in superconducting resonators by surface treatment and deep etching of silicon substrates", Appl. Phys. Lett. **106**, 182601 (2015).

[49] I. M. Pop, T. Fournier, T. Crozes, F. Lecocq, I. Matei, B. Pannetier, O. Buisson, and W. Guichard, "Fabrication of stable and reproducible submicron tunnel junctions", Journal of Vacuum Science & Technology B **30**, 010607 (2012).

[50] P. J. Petersan and S. M. Anlage, "Measurement of resonant frequency and quality factor of microwave resonators: Comparison of methods", Journal of Applied Physics **84**, 3392 (1998).

[51] N. Pompeo, K. Torokhtii, F. Leccese, A. Scorza, S. Sciuto, and E. Silva, in *2017 IEEE International Instrumentation and Measurement Technology Conference (I2MTC)* (2017), pp. 1–6.

[52] M. Reagor, H. Paik, G. Catelani, L. Sun, C. Axline, E. Holland, I. M. Pop, N. A. Masluk, T. Brecht, L. Frunzio, M. H. Devoret, L. Glazman, and R. J. Schoelkopf, "Reaching 10 ms single photon lifetimes for superconducting aluminum cavities", Appl. Phys. Lett. **102**, 192604 (2013).

[53] A. Bruno, G. de Lange, S. Asaad, K. L. van der Enden, N. K. Langford, and L. DiCarlo, "Reducing intrinsic loss in superconducting resonators by surface treatment and deep etching of silicon substrates", Appl. Phys. Lett. **106**, 182601 (2015).

[54] C. Müller, J. H. Cole, and J. Lisenfeld, "Towards understanding two-level-systems in amorphous solids: insights from quantum circuits", Rep. Prog. Phys. **82**, 124501 (2019).

Acknowledgments

Finally I want to thank everybody who supported me in conducting and writing this master's thesis.
First of all I need to express my gratitude to my supervisor Dr. Frank Deppe, who provided me the possibility to write this thesis at the WMI. Due to his experience and know-how he has always been a great help.
Also great thank applies to the people of the in-house workshop, who actually built the designed horseshoe cavity of this thesis. Thanks for preparing plenty of commercial antennas until the soldering procedure of the gold wire finally worked.
Special thanks go to Stephan Trattnig who introduced me to the workflow in the lab, the measurement electronics and the control program on the computer. He was always available for questions and helpful discussions. At this point I also want to thank Matti Partanen for the collaborative work with the cryostat and for taking over one or the other night shift. He always had an open ear for questions and I enjoyed the nice conversations.
Furthermore my office mates Florian, Leander, Manuel, Raffael, Stephan, Elisabeth, Korbinian and Christopher deserve great thanks for all the funny and encouraging coffee and lunch breaks. This gratitude certainly also goes to all the other people at WMI who attended these nice conversations.
Besides the comfortable atmosphere at WMI I also want to thank my parents and my friend Lars for their mental support during this thesis.